

Gas contamination and mitigation in a 100 m³ / 10 bar argon TPC with optical readout: a viability study

D. J. Fernández-Posada,^{a,b} D. González-Díaz,^{a,*} J. Baldonado,^b J. Collazo,^b E. Casarejos,^b P. Hamacher-Baumann,^c P. Amedo,^a J. Llerena^a

^a*Instituto Galego de Física de Altas Enerxías, Univ. de Santiago de Compostela, Campus sur, Rúa Xosé María Suárez Núñez, s/n, Santiago de Compostela, 15782, Spain*

^b*CINTECX, Universidade de Vigo, Dpt. Mech. Engineering, 36310 Vigo, Spain*

^c*III. Physikalisches Institut, RWTH Aachen University, 52056 Aachen, Germany*

E-mail: diego.gonzalez.diaz@usc.es

ABSTRACT: Gaseous Optical Time Projection Chambers (OTPCs) aimed at Neutrino Physics and Rare Event Searches will likely exceed the tonne scale during the next decade. This will make their performance sensitive to gas contamination levels as low as 100 ppb, that is challenging at room temperature due to outgassing from structural materials. In this work we discuss gas distribution and impurity mitigation on a 5 m-length/5 m-diameter 10 bar TPC filled with Ar/CF₄ admixed at 99/1 per volume (1.75 tonne), loaded with technical plastics in order to enhance light collection and readout. Different distributor topologies, outgassing and flow rates are discussed. Specifically, our work is aimed at illustrating the conceptual viability of the optical readout of ND-GAr's TPC (within the DUNE Near-Detector complex), in terms of material compatibility. For our proposal, with perforated distributors aligned with the electric field, and under realistic assumptions, the concentration of contaminants can be controlled within a week from chamber filling. In the case of N₂, injection of fresh gas at %-level seems to represent the safest strategy to keep the concentration within operability limits.

KEYWORDS: Gaseous detectors; Time projection Chambers; Outgassing; CFD simulations; Optical Readout

Contents

1	Introduction	1
2	Inputs	3
2.1	Impact of impurities on TPC response	3
2.2	Outgassing model	7
2.3	Gas distribution scheme	9
3	Fluid dynamics model	11
3.1	Optimization of the distributor rods	11
3.2	CFD simulations	15
4	Results	17
4.1	TPC filling	17
4.2	Oxygen contamination	18
4.3	Water contamination	20
4.4	Nitrogen contamination	23
5	Summary and conclusions	25
A	Iterative implementation of a multi-hole distributor	29
B	Useful analytic limits for capped distributors	30
C	Time-dependent differential equations	31
C.1	Constant outgassing rate	31
C.2	Power-law outgassing rate	32
C.3	Gas displacement during filling	33
C.4	Gas accumulation	33

1 Introduction

Gas distribution and purification, together with material selection, are crucial aspects for the operation of gaseous instrumentation (e.g., [1]). With future large-volume detectors poised to reach the tonne scale in gas mass for the first time, the associated challenges will increase, particularly in the form of time projection chambers, or TPCs [2–4]. As an example, the DUNE experiment (dedicated to the study of neutrino oscillations) is considering the construction of a nearly 2 tonne argon-rich TPC that would operate at 10 bar, with 5 m diameter and 5 m drift (as part of the ND-GAr detector [5, 6]); the NEXT experiment (targeting the discovery of $\beta\beta 0\nu$) aims at a bit over 1 tonne of ^{136}Xe in a 15 bar TPC of 2.6 m (diameter) \times 2.6 m (drift) [7]; CYGNUS-1000 (whose goal is the reconstruction of the direction of galactic WIMP dark matter) plans operation

under He/SF₆(CF₄) at around atmospheric pressure in a 1000 m³ detector, totaling 3 tonne [8]. The need for such unprecedented masses of gas is driven by the unique capability of this phase to resolve the details of the interactions involving low-energy particle tracks, provided a sufficient interaction/decay probability can be guaranteed in the first place.

There are, as well, contemporary elements that further complicate the design at this new scale: some of the gases considered (e.g., SF₆, CF₄) represent a threat to the environment,¹ while others (e.g., ¹³⁶Xe) are too precious to be vented. This enforces operation in closed-loop, thereby binding the system performance to the power of the compressors and purification systems, in competition with the outgassing rate from internal elements. When high gas mass is achieved through pressurization, the attachment probability (electron lifetime) is increased (decreased) as $\sim P^2$ [10] and both charge collection and mm-level space resolutions can be compromised even in the presence of tiny concentrations of contaminants. As shown in this work, the sensitivity of the drift velocity to impurities, combined with experimental values of the attachment coefficient, set the tolerable H₂O and O₂ levels at the 0.1-1 parts per million (ppm) scale for $O(10\text{ m})$ drift. This is at least one order of magnitude below the purity requirements of the ALICE TPC, the largest gaseous TPC to date [11].

Simulations based on computational fluid dynamics (CFD) are nowadays possible in a variety of systems. As they provide critical information on the flow characteristics and the admixing of species, they can reduce the investment in physical prototypes and help anticipating problems. CFD simulations of gaseous detectors usually focus on characteristics of the gas flow such as gas stagnancy ('pockets') and the impact of temperature gradients, since they modify the detector response locally [12]. However, not much has been done to address the role of contaminants, to the best of the authors' knowledge. Modeling the dynamics of contaminants in fluid detectors is not alien to modern technologies, and it has been successfully done for instance for liquid argon TPCs based on a set of differential equations describing each of the elements in the system [13].

In this work we study gas distribution and impurity mitigation in the context of future large volume/large mass TPCs intended for experiments in the field of Neutrino Physics and Rare Event Searches. We discuss, in particular, a scenario where a massive use of technical plastics would be made in order to enhance the optical response of a TPC aiming at the study of neutrino interactions, following the conceptual proposal outlined in [14]. A distributor geometry based on axial rods has been chosen as the baseline, although other gas distribution concepts are possible (e.g. through forced axial flow). Axial distribution rods have the advantage of being a priori amenable to any field-cage design and little dependent on the end-cap details.

The structure of this document is as follows. First, section 2 discusses the main inputs used in the CFD simulations: (2.1) the influence of contaminants on the TPC response, obtained from existing data or electron-transport simulations; (2.2) outgassing rates of technical plastics; and (2.3) gas distribution scheme. Section 3 deals with the optimization of the geometry of the distributor rods (3.1), and the introduction of the CFD simulation framework (3.2). Section 4 presents our main results, chiefly the spatial and temporal distributions of common outgassing species in the TPC for different distribution schemes, species and conditions. Finally, we end with our conclusions in section 5.

¹Available estimates of the global warming potential (GWP) exceed 20000 for SF₆ and 5000 for CF₄, [9].

2 Inputs

We adopt a reference geometry of a 5 m-length/5 m-diameter cylindrical TPC, as that currently under consideration for DUNE’s ND-GAr ([5, 6]), intermediate in size with respect to [7] and [8]. The recently introduced possibility of performing ‘Full3D’ optical tracking in Ar/CF₄ (99/1) [14–17], involves the use of large amounts of reflective (Teflon) and transparent (PMMA) plastics, to enhance the optical response of the detector. That extreme situation (in terms of system outgassing) is discussed in the following. A scheme of the system, together with a conceptual gas distribution scheme, can be found in Fig. 1.

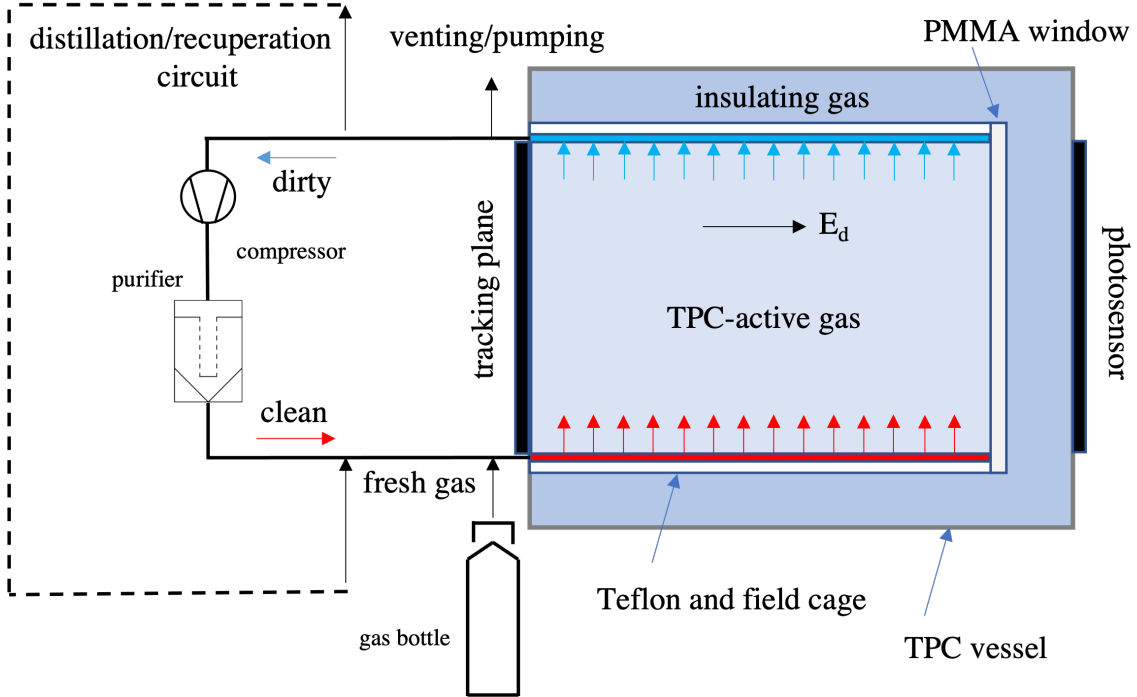


Figure 1. A minimalistic concept of the gas distribution proposed for DUNE’s ND-GAr, containing the main elements discussed in text. Manual and automated valves, probing points to assess the gas concentration (and possibly purity), as well as pressure and vacuum gauges will be needed in the final implementation. An additional insulating layer based on gas has been foreseen, acting as electrical (for the field cage) and thermal (for the photosensor) barriers. The full concept will be discussed elsewhere.

2.1 Impact of impurities on TPC response

Contaminants such as H₂O, O₂ and N₂ will be considered, since they are predominantly found in the outgassing of materials with low vapour pressure (i.e., barring most epoxies and adhesives from detector construction). We neglect contamination from exogenous impurities arising for instance from residual gas in the bottles, that might be pernicious at concentrations much below the ones discussed in this work [18]. Contaminants such as CO₂ and CO can be also found, e.g. for technical plastics [19], at outgassing rates similar to those of the aforementioned species. An upper limit to their impact on the chamber performance can be obtained from the analysis made in this section for the case of H₂O, since the latter displays one of the strongest electron-cooling powers of the

molecules discussed: this means, namely, a larger distortion of the drift of the primary ionization electrons compared to the purified gas. The main mechanisms through which impurities can limit the performance of a TPC are: i) the capture of the drifting electrons (attachment) and ii) the alteration of the drift velocity and the ensuing track distortions, affecting momentum reconstruction. For TPCs relying on scintillation, as discussed here, iii) modifications to the scintillation probability and absorption can occur too.

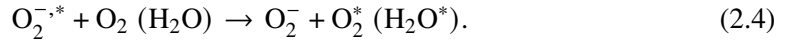
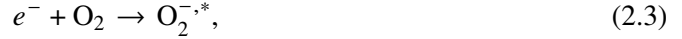
Reference values for the contaminant thresholds as used in this paper can be determined by examining the effects in attachment, drift velocity and light quenching and absorption, as follows:

- Attachment: of utmost importance at high pressure is the attachment probability per unit length for electrons drifting in the presence of oxygen (η), or its related magnitude: the electron lifetime (τ_e). For argon-based mixtures those may be parameterized, after [10], as:

$$\eta = \frac{1}{v_d} \cdot \left(1 + \frac{f_{H_2O}}{1000}\right) \cdot P^2 \cdot f_{O_2} \cdot \mathcal{A}_{\text{gas}}, \quad (2.1)$$

$$\tau_e = \frac{1}{\eta \cdot v_d}, \quad (2.2)$$

where the magnitude \mathcal{A}_{gas} is gas-mixture dependent, $f_{O_2(H_2O)}$ represents the volume concentration of O_2 (H_2O), v_d is the electron drift velocity and P is the gas pressure. The P^2 -dependence reflects the fact that the dominant attachment process takes place in two steps (Bloch-Bradbury-Herzengber mechanism, BBH, [20, 21]):



Both \mathcal{A}_{gas} and v_d depend solely on the pressure-reduced electric field (E/P), therefore not showing separate E and P dependencies.² Typical pressure-reduced drift fields in TPCs are found in the range of 10 – few 100's V/cm/bar, expectedly below the dissociative-attachment thresholds for either CF_4 , O_2 or H_2O . This observation has been backed with the state-of-the-art Pyboltz transport code [22], thus anticipating BBH to be the dominant attachment mechanism in the conditions discussed in this work.

The attachment coefficient, η , in Ar/ CF_4 (99/1) at $E/P = 100$ V/cm/bar might be estimated starting from the experimental \mathcal{A}_{gas} value in case of the classical Ar/ CH_4 mixture at 90/10 ('P10'). The compilation in [10], performed up to 4 bar, indicates that $\mathcal{A}_{\text{gas}} = 15.1 \pm 1.5 \mu\text{s}^{-1}$, and $v_d = 5.36$ cm/ μs . Extrapolating to 10 bar following eq. 2.1, this value would correspond to 10% charge loss over 5 m drift for O_2 concentrations of 0.7 ppm. The same work reports a linear decrease of \mathcal{A}_{gas} with the decrease of the concentration of the molecular additive and an increase with the size of the molecule (e.g., from CH_4 to $i-C_4H_{10}$). The effect can be attributed to the dependence of the stabilization reaction 2.4 with the concentration of the molecular additive and with the molecule size. For Ar/ $i-C_4H_{10}$ at 99/1, $\mathcal{A}_{\text{gas}} = 48.4 \pm 3.7 \mu\text{s}^{-1}$ and $v_d = 4.97$ cm/ μs were measured at $E/P = 100$ V/cm/bar, yielding a 10% charge drop over 5 m for 0.2 ppms of O_2 . Given that $i-C_4H_{10}$ and CF_4 molecules are similar in size, a similar strength of reaction 2.4, and thus similar attachment rates, might be expected.

²This is a direct consequence of the fact that E/P determines uniquely the electron energy distribution.

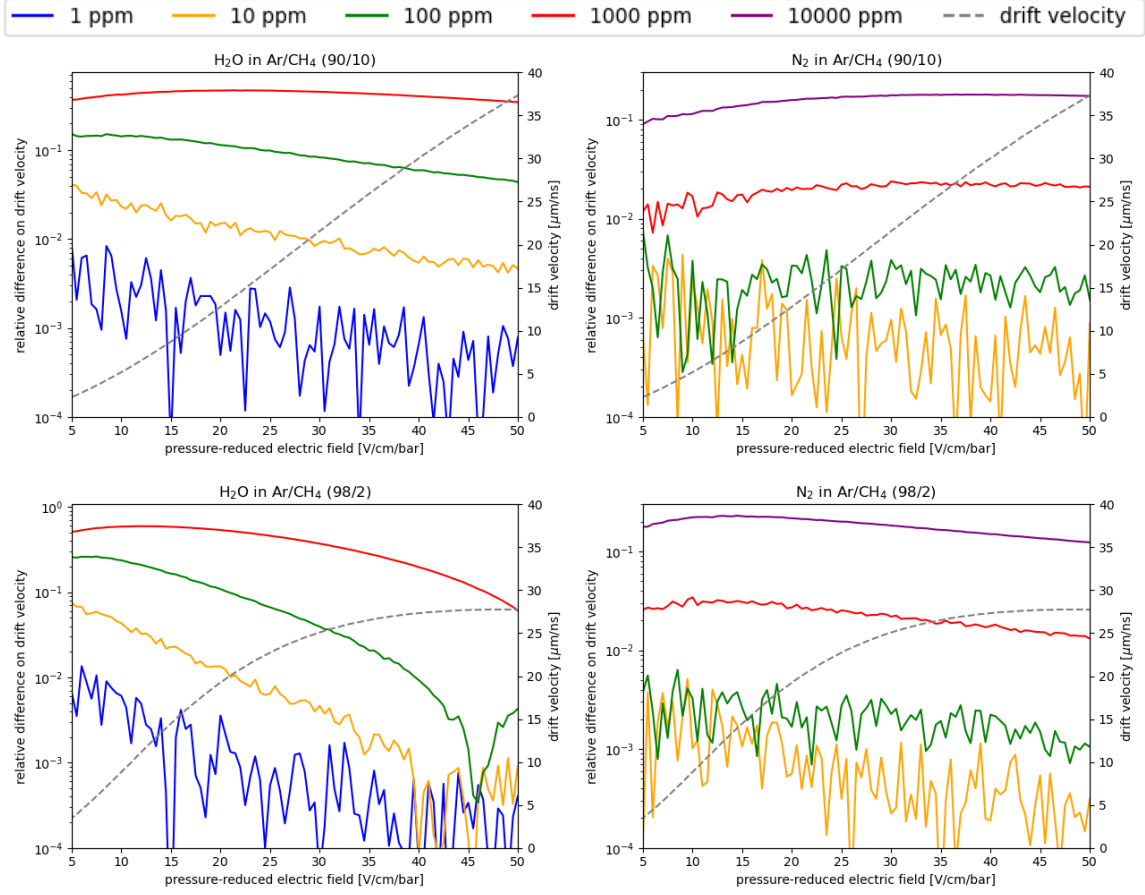


Figure 2. Relative variation of the drift velocity (v_d) with respect to purified conditions, for different impurity concentrations (absolute value). Simulations have been performed with Pyboltz, focusing on Ar/CH₄ admixtures at $P = 10$ bar and $T = 25$ °C. The top two figures correspond to Ar/CH₄ admixed at 90/10 (P10) and the bottom two to Ar/CH₄ at 98/2. Left: H₂O contamination. Right: N₂ contamination. Drift velocity is also shown (dashed line) with axis on the right.

An E/P of 100 V/cm/bar would correspond to an imposing 500 kV cathode bias on a 5 m drift distance at 10 bar. Based on the studies of breakdown voltage for Ar/CF₄ (99/1) carried out in [23], as well as the availability of commercial feedthroughs, we will restrict our discussion to a cathode bias not greater than 250 kV ($E/P = 50$ V/cm/bar). That would roughly double the value of \mathcal{A}_{gas} compared to $E/P = 100$ V/cm/bar, extrapolating from [10]. Based on this, we aim in this work for an O₂ concentration value not larger than 0.1 ppm, so as to keep the charge losses well within 10%.

- Modifications of the drift velocity: impurities, even in trace-amount, can substantially modify the drift velocity to the extent of limiting particle tracking, too. Fig. 2 provides the sensitivity of Ar/CH₄ (90/10) to H₂O (left) and N₂ (right), as a function of the pressure-reduced electric field in the range 5-50 V/cm/bar. It represents the magnitude $\left| \frac{\Delta v_d}{v_d} \right| = \left| \frac{v_d(f=0) - v_d(f)}{v_d(f=0)} \right|$, obtained with Pyboltz at $P = 10$ bar and $T = 25$ °C. The figure shows how, as expected, the impact of H₂O is stronger than that of N₂ by at least one order of magnitude.

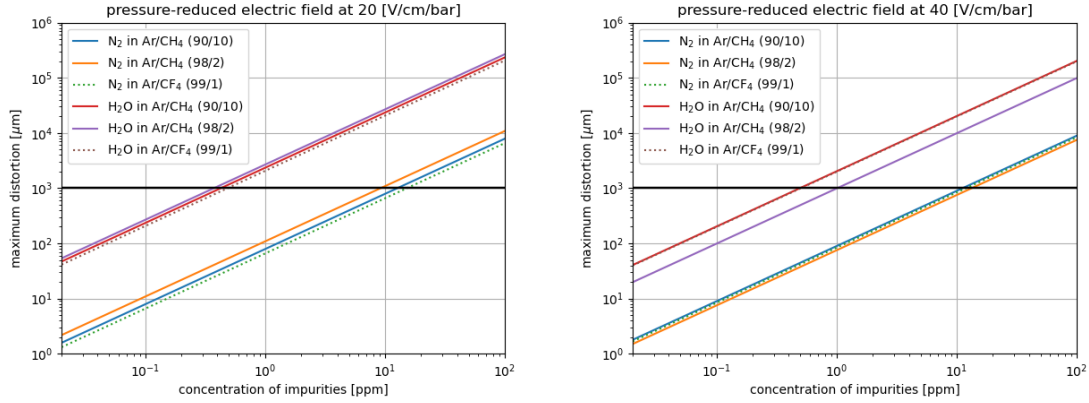


Figure 3. Maximum track distortion obtained in simulation as a function of the concentration of contaminants in the gas medium, at 10 bar and a temperature of 25 °C. The pressure-reduced electric field is 20 V/cm/bar (left) and 40 V/cm/bar (right). Three reference gas mixtures are considered (Ar/CH₄ at 90/10 and 98/2, Ar/CF₄ at 99/1), under H₂O and N₂ contamination (the case of O₂ is not shown, for clarity, but it is similar to N₂).

Deviations from the nominal (impurity-free) value of the drift velocity will cause distortions on the reconstructed tracks. We assume here a worse-case scenario where the standard calibration systems (e.g.: laser [24], ^{83m}Kr source [25], online drift-monitor [26], cosmic muons...) either do not exist or are not able to perform the required corrections fully. In such a case, a track close to the cathode would yield a misreconstructed axial position by as much as:

$$\Delta z = L \left| \frac{\Delta v_d}{v_d} \right| \approx \frac{L}{v_d(f=0)} \cdot \left| \frac{dv_d}{df} \right| \cdot f \quad (2.5)$$

with $L = 5$ m being the drift distance. The linear approximation on the r.h.s. of eq. 2.5 allows extrapolation to low concentrations (f), for which the numerical precision of simulations is lost. Fig. 3 presents the maximal track distortion as a function of the concentration of impurities (from eq. 2.5) for two typical electric fields (200 V/cm, 400 V/cm) and three gas mixtures (Ar/CH₄ at 90/10 and 98/2, and Ar/CF₄ at 99/1). For reference, the 1 mm space-resolution landmark is indicated with a horizontal line. As seen, depending on the system requirements, the tolerable impurity levels range from 10 ppms of N₂ (1 mm distortion) down to values as low as 0.05 ppms of H₂O (0.1 mm distortion). The case of O₂ is not shown since the contamination levels that are acceptable for tracking are well above those for H₂O and, in most practical conditions, its presence will impact the electron lifetime much before it starts to be a concern for tracking. The tolerable concentrations of contaminants that will be assumed throughout this work will be 10 ppm for N₂ and 1 ppm for H₂O (limited by distortions in tracking at mm-level) and 0.1 ppm for O₂ (limited by attachment). They are compiled in table 1.

- Light quenching and absorption: light quenching (preceding emission) and absorption (following emission) depend strongly on the gas mixture. For reference, pure Ar scintillation peaks in the vacuum ultraviolet (VUV) at around 128 nm [27], and photoabsorption coef-

ficients (at around room temperature) can reach in this region values as large as $\Pi = 100 \text{ cm}^{-1} \text{ bar}^{-1}$ for common impurities [28]. With light attenuation following the absorption law $\sim \exp(-L \cdot P \cdot f \cdot \Pi)$, a 10% light loss on $L=5 \text{ m}$ of argon at $P=10 \text{ bar}$ would roughly arise from just 0.2 ppm of any common contaminant. The slow decay times of the triplet component of Ar_2^* ($\tau_3 = 3.2 \mu\text{s}$), on the other hand, make argon scintillation very vulnerable to deactivation transfer reactions (quenching) with impurities, too. The ‘triplet-dominance model’ describes well the situation in conditions of interest to gaseous detectors [29, 30], leading to an expression for the light loss:

$$P_Q = 1 - P_{\text{scin}} \approx 1 - \frac{1}{k \cdot P \cdot f \cdot \tau_3} \quad (2.6)$$

Here P_{scin} is the scintillation probability, k the quenching rate in units of bar^{-1} , and f is the fraction of contaminant. Measurements of the scintillation quenching in [29] point to 0.2 ppm as the concentration at which CO_2 would cause 10%-level light losses, and about 20 ppm for N_2 (at 10 bar pressure).

The experimental values obtained above, for the maximum concentrations of impurities that are compatible with argon scintillation, are at the same level (or even below) than those obtained from the analysis of the charge properties in regard to attachment and drift velocity. The situation for Ar/CF_4 (99/1) is expected to be much more favourable, though. First, about 90% of the usable scintillation lies in the near-UV and visible range (200-800 nm) in that case [16, 31]. Considering the absorption coefficient for H_2O at the low-end of such wavelength range, a value of $\Pi = 10^{-2} \text{ cm}^{-1} \text{ bar}^{-1}$ is expected [28]. As a result, 10%-level light losses would require of H_2O concentrations as high as 200 ppms (being water the most opaque contaminant, a priori). Regarding light quenching, it has been measured in [32] for pure CF_4 at 1 bar to be 50% under a N_2 contamination of 4%. Assuming a quenching relation of the type 2.6, 4000 ppms of N_2 would be needed to cause a 10% light loss. The factor 200 above the values obtained for pure argon matches well the expectation in eq. 2.6 resulting from the much shorter lifetime of CF_4 states, in the range 10-20 ns [15]. Following the analogy with the argon case further, a plausible estimate of the maximum amount of (more reactive) molecules such as CO_2 and H_2O would be 40 ppms, greatly exceeding the upper bounds obtained from charged transport.

2.2 Outgassing model

Outgassing is dominated by the technical plastics employed in TPC construction, that is orders of magnitude above that of metals, e.g., from the TPC vessel or field cage. We consider Teflon (commonly used as a light reflector and as a structural material for field cages [33, 34]), PMMA (a sturdy material with good optical properties) and PEEK (a low-outgassing structural material). Plastics follow, in general, an outgassing law depending on time (t) as $Q(t) \sim t^{-a}$ with $a \sim 1/2$, corresponding to a diffusion-driven bulk desorption law. This is in principle applicable as long as i) the desorbed gas remains far from the saturation concentration of the exterior (about $f = 3000 \text{ ppm}$ in case of H_2O at $T=25 \text{ }^\circ\text{C}$, $P=10 \text{ bar}$) and ii) the material is thick enough to keep furnishing the contaminant at any given time. As time passes, however, the desorbed gas reaches out from deeper regions until the material boundaries are approached, moment at which outgassing drops

exponentially. The process leads to the following piece-wise outgassing law [35]:

$$Q(t) = \begin{cases} k\sqrt{\frac{\pi\tau}{t}} & \text{for } t \leq 0.5\tau, \\ 4k e^{-t/\tau} & \text{for } t > 0.5\tau. \end{cases} \quad (2.7)$$

Here, k indicates the strength of the outgassing rate and τ is the time constant that characterizes the moment at which the depth-of-origin of the desorbed species approaches the material thickness t_m . It is computed as $\tau = \frac{t_m^2}{\pi^2 D_{\text{bulk}}}$, with D_{bulk} being the diffusion coefficient in the bulk. A typical value for technical plastics is $D_{\text{bulk}} = (3.0 \pm 1.2) \times 10^{-9} \text{ cm}^2 \text{ s}^{-1}$, following [36].

Outgassing rates are usually obtained in vacuum, and they can be parameterized through the value measured 10 hours after pumping (Q_{10h}) and the exponent a [37] (the latter assumed to be 0.5 hereafter). For instance, in the case of Teflon at room temperature, Q_{10h} varies typically from 3.5×10^{-8} to $1 \times 10^{-7} \text{ mbar} \cdot \text{l} \cdot \text{cm}^{-2} \cdot \text{s}^{-1}$ (for a recent review, see [38]). Mass spectroscopy indicates that the outgassing content in O_2 is generally less than 10% of the total while N_2 and H_2O concentrations vary much more, going from nearly 70% H_2O and 30% N_2/CO to nearly 100% N_2 and 0% H_2O [19, 37, 39]. For both H_2O and N_2 we will consider the most unfavourable case (i.e., that they constitute 100% of the outgassing), together with the middle ('typical') and lowest ('optimistic') Q_{10h} values obtained for the total outgassing rates in [38]. For O_2 we take a range comprised between the value directly measured in [19] ('optimistic') and 10% of the middle value of Q_{10h} in [38] ('typical'). As outgassing rates depend on the material quality and surface finish, the rationale for our choice has been to select a range that includes typical outgassing values as well as the lowest ones found in literature. Measurements in [19] are important, as they do not involve bake out, thereby matching the expected experimental conditions under which large-volume TPCs are commissioned.

Outgassing rates for PMMA and PEEK, on the other hand, are found in the range $Q_{10h} = 10^{-7} - 10^{-6} \frac{\text{mbar} \cdot \text{l}}{\text{cm}^2 \cdot \text{s}}$. In the former case, they tend to be dominated by H_2O , without any trace of O_2 or N_2 being found (e.g., [19]). In the latter, the situation is similar however the amount of O_2 reported in literature is %-level (e.g. [40]). Assuming PMMA to be typically used as a window for light detection [41] and PEEK to be sometimes present in readout frames [42], one can anticipate that the use of these materials would be restricted to the end-caps, constituting a 20% of the total outgassing surface (at maximum) in our default geometry. Thus, the contribution of PMMA and PEEK to outgassing can be made generally subdominant in the presence of a Teflon reflector, if the former materials are chosen in the lower-end of the range of measured values.

In the following, we will adopt the outgassing law in eq. 2.7 for studying the impact of H_2O and N_2 in the TPC performance. For O_2 (a priori the most critical case), we will perform the calculations assuming a more extreme scenario in which the outgassing remains constant at $Q = Q_{10h}$. In all cases, Teflon will be assumed to dominate the system outgassing. A compilation of the outgassing rates considered in this work can be found in table 1 (column 2).

Once the outgassed species reach the material surface, further diffusion into the exterior volume will be suppressed depending on the gas pressure. The diffusion coefficient of species 'x' ($x \equiv \text{O}_2, \text{H}_2\text{O}, \text{N}_2$) in a given gas (helium, neon, argon and xenon will be considered here) can be evaluated

species	$Q_{10h} [\frac{\text{mbar}\cdot\text{l}}{\text{cm}^2\cdot\text{s}}]$	model	ppms	$D_{x,\text{Teflon}} [\text{cm}^2/\text{s}]$	$D_{x,\text{He/Ne/Ar/Xe}} [\text{cm}^2/\text{s}]$
O ₂	$(0.05 - 1) \times 10^{-8}$	const.	~ 0.1	$(3 \pm 1.2) \times 10^{-9}$	0.0725 / 0.0316 / 0.0195 / 0.0126
H ₂ O	$(0.35 - 1) \times 10^{-7}$	$t^{-1/2}$	~ 1	$(3 \pm 1.2) \times 10^{-9}$	0.084 / 0.0397 / 0.0252 / 0.0173
N ₂	$(0.35 - 1) \times 10^{-7}$	$t^{-1/2}$	~ 10	$(3 \pm 1.2) \times 10^{-9}$	0.0692 / 0.0310 / 0.0194 / 0.0128

Table 1. Lower (‘optimistic’) and upper (‘typical’) limits to the Teflon outgassing rates considered in this work, for different gas species. A $Q \sim Q_{10h} \cdot \sqrt{t/10h}$ law has been assumed for H₂O and N₂, and a conservative $Q \sim Q_{10h}$ law for O₂ (third column). The fourth column shows the typical limiting concentrations for TPC operation under argon gas at 10 bar, as obtained in text. The fifth column provides an estimate of the effective diffusion constant of the outgassed species in Teflon. Finally, the last column compiles the diffusion constants of typical outgassed species ($x = \text{O}_2, \text{H}_2\text{O}, \text{N}_2$) in helium, neon, argon and xenon gas at $P = 10$ bar and $T = 20$ °C.

following a formula based on Fuller’s work [43, 44] as:

$$D_{x, \text{He/Ne/Ar/Xe}} = \frac{0.00143 \cdot T^{1.75}}{P \sqrt{\frac{2}{\frac{1}{M_x} + \frac{1}{M_{\text{He/Ne/Ar/Xe}}}}} \cdot [\sqrt[3]{V_x} + \sqrt[3]{V_{\text{He/Ne/Ar/Xe}}}]^2}, \quad (2.8)$$

in units of cm²/s. Here M is the molecular mass of each gas, P is the pressure in bar, T is the temperature in K, and V_i are non-dimensional ‘experimental diffusion volumes’. The expression above can be evaluated for admixtures ($B_1 + B_2$), as long as contaminants remain at concentrations much below those of the gas constituents:

$$\frac{P}{D_{x, B_1+B_2}} = \frac{P_{B_1}}{D_{x, B_1}} + \frac{P_{B_2}}{D_{x, B_2}}. \quad (2.9)$$

In the above equations, P_i represent the partial pressures of each gas in the mixture. Diffusion volumes can be extracted from [44]: $V_{\text{Ar}} = 16.2$, $V_{\text{H}_2\text{O}} = 13.1$, $V_{\text{N}_2} = 18.5$, $V_{\text{O}_2} = 16.3$, $V_{\text{CH}_4} \simeq V_C + 4V_H = 25.1$, $V_{\text{Xe}} = 32.7$, $V_{\text{He}} = 2.67$, $V_{\text{Ne}} = 5.98$ and $V_{\text{CF}_4} \simeq V_C + 4V_F = 74.7$. For the admixtures discussed in this work, the diffusion coefficients are sufficiently close to those in the main gas so that we may neglect the contribution from the molecular additive (a compilation can be found in table 1, last column).

It should be noted that it is in principle possible that additional mechanisms at the material-gas interface could introduce a pressure dependence and an outgassing law different from the one assumed in vacuum. This would need to be elucidated through direct measurements. As for other assumptions employed earlier in text, the aim of our study is to provide upper limits to the impact of impurities in an actual system, and verify that they can be brought below potentially harmful levels through reasonable design choices. Along this direction, there is no obvious mechanism by which outgassing could be enhanced as pressure increases, compared to the model proposed here.

2.3 Gas distribution scheme

Our baseline proposal for the gas distribution is based on axial rods (perforated plastic tubes) attached to the field-cage, the inlets being at the bottom-half and the outlets at the top-half, as shown in Fig. 4 (top-left). The rationale for this choice is to allow a simple implementation since the field-cage is generally the less instrumented part of a TPC. Thus, this concept does not interfere

with the end-cap design and, with sensible choices, it can assure uniform gas distribution along the drift/axial direction. Sixteen equispaced axial rods run along the rectangular section of the TPC (eight for injection and eight for extraction) as shown in Fig. 4 (top-right), providing an inter-rod distance of nearly 1 m between the centers. As shown later, this is sufficient to sweep the outgassing from the field-cage walls efficiently. The distributor rods are periodically perforated with a pattern that is discussed in the next section.

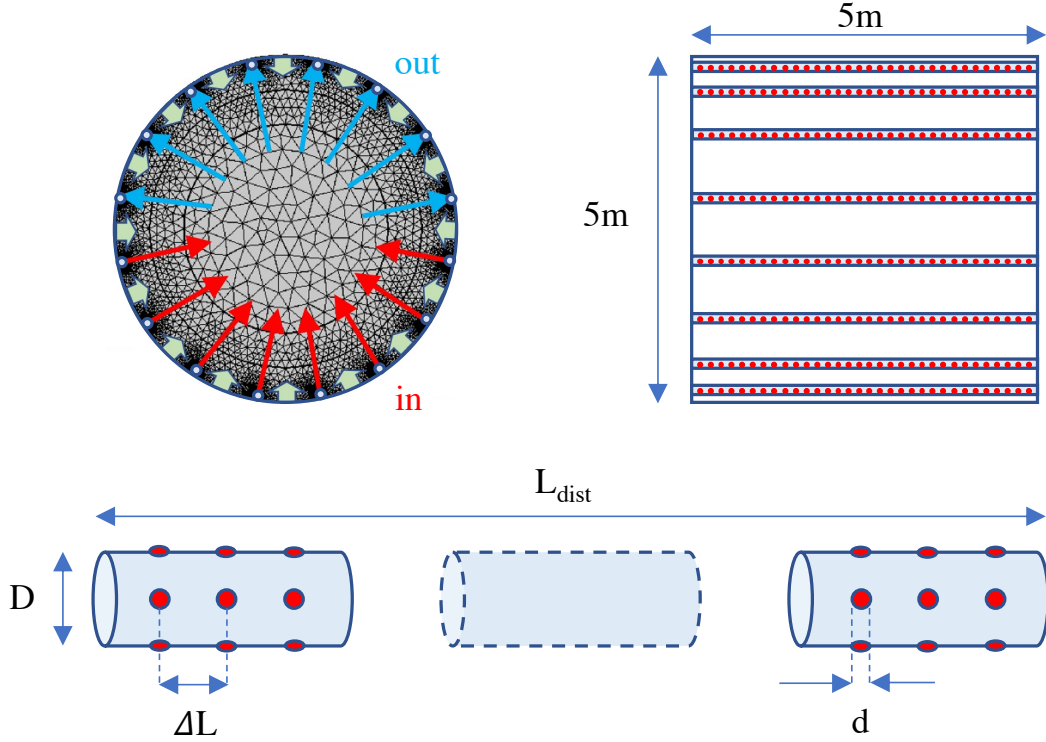


Figure 4. Top: cross-section of the proposed gas distribution inside the field cage (left), with perforated distribution rods extending axially along it (right). Eight injection rods are placed at the bottom and eight ejection rods at the top. The field cage is assumed to be gas-tight, extending along 5 m in length and 5 m in diameter. Holes are indicated by circles (not to scale). Bottom: close-up of a gas distributor rod.

It is assumed that the gas is continuously recirculated through compressors that, in combination with purifiers (getters), can keep the injected gas clean at all times. Commercial ‘cold’ getters are capable of maintaining O_2 and H_2O concentrations at ppb-level per pass, being at the same time oblivious to common molecular additives such as CH_4 and CF_4 . In simulation, as the purification levels are at least two orders of magnitude below the concentrations considered to be harmful, we will assume that the injected gas is at all times 100% pure. On the other hand, getters capable of trapping N_2 need of heating, that may cause incompatibility with high gas flows as well as with the use of molecular additives. When studying nitrogen contamination in text, we will not consider the possibility of purification.

Given the above conditions, and in the absence of gas leaks, the ultimate purity levels that can be achieved are limited by the power of the recirculation compressors. For reference, the ALICE

TPC circulates gas at 20 m³/h (1 bar) while the NEXT-100 experiment is designed to circulate at around 5 m³/h (10 bar), [45]. Based on this, we will consider two different conditions for a 10 bar system, referring to them as ‘typical’ (30% above NEXT flow: 6.5 m³/h) and ‘optimistic’ (20 m³/h), as summarized in table 2.

3 Fluid dynamics model

We discuss, separately: i) the optimization of the geometry of the distributor rods, performed through a parametric model based on generalized continuity equations and ii) the CFD simulations of the proposed gas distribution scheme, focusing on the concentrations of contaminants in space and time, performed with COMSOL Multiphysics v5.5 [46] (‘Fluid Flow’ Module).

3.1 Optimization of the distributor rods

Results from a three-dimensional CFD simulation performed, illustratively, for a 3-hole distributor, are shown in Fig. 5. It provides a cross-section at the holes’ middle plane (the modulus of the gas velocity is represented on the left column, the pressure profile on the right one). Two reference cases are considered: a capped distributor (top) and an open one (bottom). As expected, an open distributor is more inefficient, given that only a fraction of the gas exits the distributor through the holes and into the chamber, as small as few % for high gas flow. It also leads to a higher pressure drop along the distributor due to friction, a far greater directionality of the outgoing gas and a non-uniform discharge pattern. Low efficiency in combination with a directional and non-uniform discharge pattern will impact the distribution of impurities throughout the chamber and the time to achieve an uniform mixing with the main gas. Therefore, we opted for a capped distributor, assuring uniform and normal injection of all the circulated gas.

A large number of holes per gas distributor, of the order of several 100’s, has been proposed in previous large-volume TPCs (e.g. [11]). Optimizing such a geometry, each hole being potentially down to $\mathcal{O}(\text{mm})$ in size, and each distributor rod extending over a length of 5 m, is impractical when using numerical simulations. As an alternative, we opted for a parametric approach based on the balance equations for each hole section, that allows to obtain the solution iteratively. We followed the classical formulation of [48], whereby: i) a discharge coefficient C_d (between 0 and 1) regulates the loss of flow into the distributor holes, — mass balance; ii) a regain coefficient C_r (between 0 and 2) regulates the pressure increase along the distributor after the ensuing velocity drop (Fig. 5-right), — momentum balance; iii) an angular coefficient γ regulates the angle of discharge relative to the normal:

$$D^2(v_{\text{up}} - v_{\text{down}}) = d^2 C_d \sqrt{\frac{\Delta P_{\text{hole}}}{\rho/2}}, \quad (3.1)$$

$$P_{\text{down}} - P_{\text{up}} = C_r \frac{1}{2} \rho (v_{\text{up}}^2 - v_{\text{down}}^2), \quad (3.2)$$

$$\theta = \gamma \cdot \arctan \left(\sqrt{\frac{\frac{1}{2} \rho v_{\text{up}}^2}{\Delta P_{\text{hole}}}} \right). \quad (3.3)$$

In the above expressions D refers to the diameter of the distributor, d is the hole diameter and ρ the gas density, whereas sub-indexes ‘up’ and ‘down’ refer to upstream and downstream of a given hole.

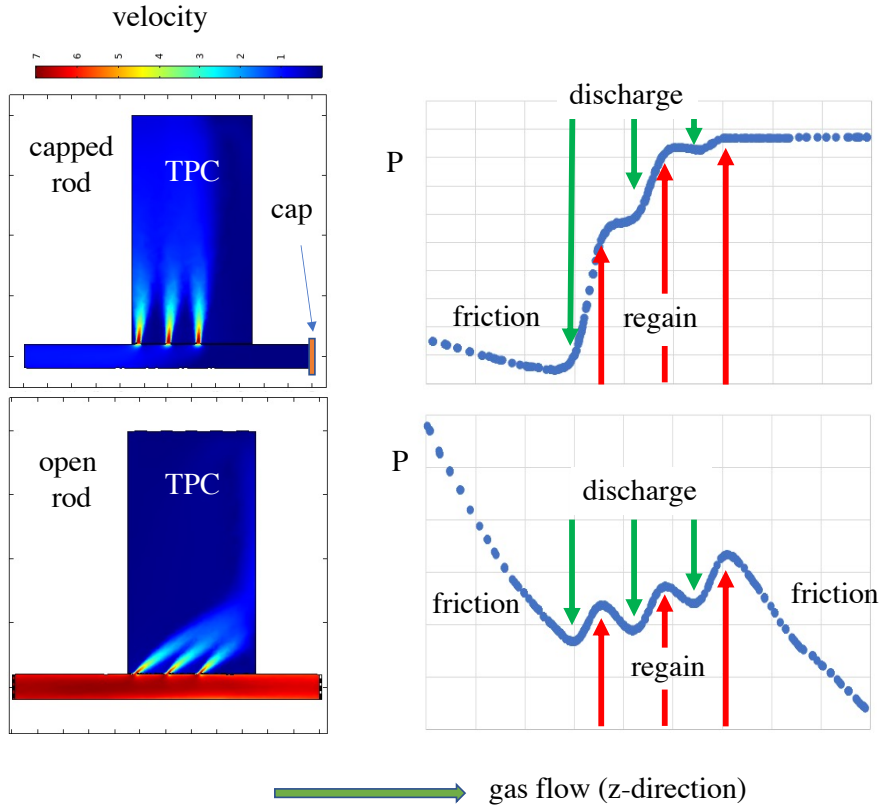


Figure 5. Left: exemplary three-dimensional CFD simulations for a 3-hole distributor (top: capped; bottom: open), representing the modulus of the gas velocity in the plane containing the holes. Right: pressure as a function of the longitudinal position, showing the discharge and regain zones. Friction dominates outside the holes' region.

Velocities (v) and pressures (P) must be understood as averages over the distributor cross-section. ΔP_{hole} is the pressure difference between the distributor and the TPC at the hole position, that drives the hole discharge:

$$\Delta P_{\text{hole}} = \frac{P_{\text{up}} + P_{\text{down}}}{2} - P_{\text{TPC}}. \quad (3.4)$$

Losses due to friction will occur when the gas transits between adjacent holes, however in the conditions discussed here the effect is negligible. For each distributor topology three main magnitudes have been evaluated through the iterative solution of the balance-equations: the pressure difference between the distributor and the TPC at the position of each hole (ΔP_{hole}), the velocity of the gas as it flows through it (v_{hole}), and its maximum discharge angle relative to the normal (θ_{max}). An example of the results obtained is presented in Fig. 6 (for details on the numerical procedure, the reader is referred to the appendix).

In the conditions studied here, as $d \ll D$ and the discharge velocity is both small and very

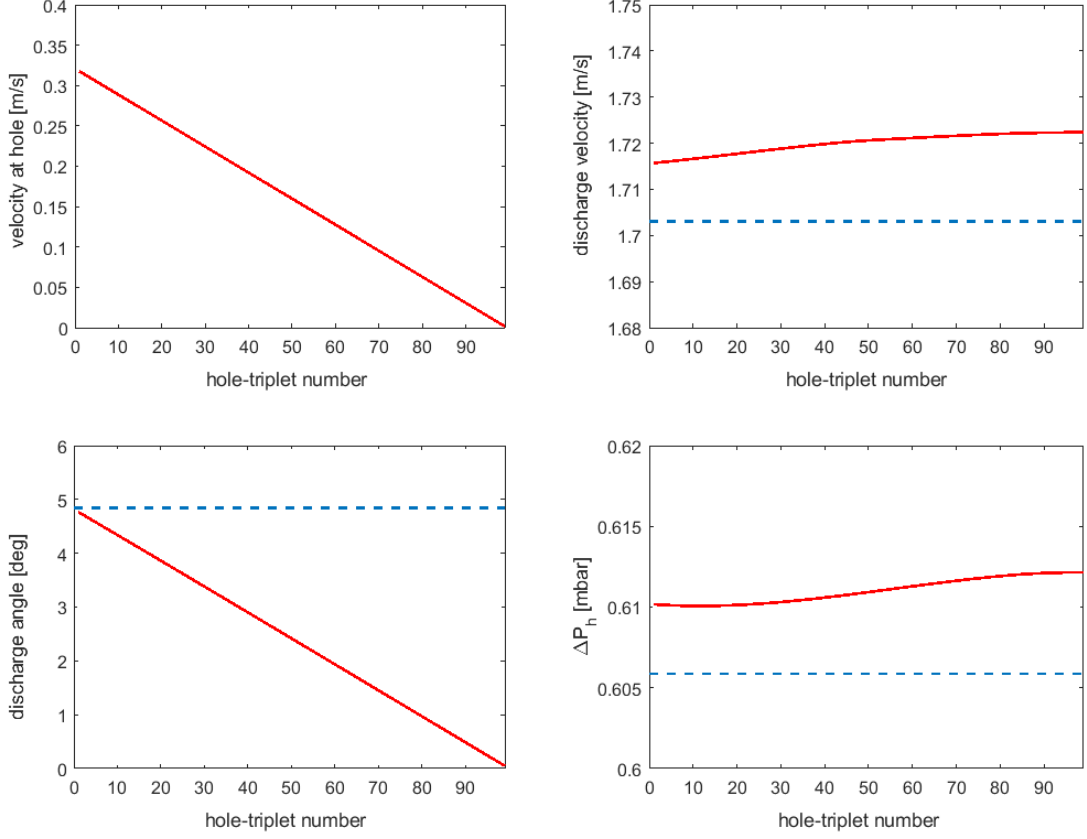


Figure 6. Main magnitudes characterizing the response of the distributor rod for each triple-hole along the distributor, shown with red lines (the first triple-hole upstream is number 1). We consider an argon gas flow of $6.5 \text{ m}^3/\text{h}$ at 10 bar, 8 distributors of 3 cm in diameter and 5 m in length. The hole size is 0.75 mm and holes are separated by 5 cm, (geometry D in table 2). Top-left: gas velocity in the distributor at the hole position. Top-right: discharge velocity. Bottom-left: angle relative to normal. Bottom-right: pressure difference relative to the TPC. (The analytical expressions given in text are shown as dashed lines).

similar for all holes, it is possible to approximate the above magnitudes by (see appendix):

$$\Delta P_{\text{hole}} \simeq \frac{1}{2} \frac{1}{C_d^2} \rho v_{\text{hole}}^2, \quad (3.5)$$

$$v_{\text{hole}} \simeq \frac{\Phi}{\text{t.h.a.}}, \quad (3.6)$$

$$\theta_{\text{max}} \simeq \gamma C_d \frac{d^2}{D^2} \frac{L_{\text{dist}}}{\Delta L}, \quad (3.7)$$

with Φ being the total gas flow injected into the TPC, t.h.a. being the total hole area, L_{dist} the length of the distributor, ΔL the distance between holes, and the total hole area relates to the number of distributors and holes per distributor as:

$$\text{t.h.a.} = N_{\text{dist}} \cdot N_{\text{holes/dist}} \cdot \frac{\pi}{4} d^2. \quad (3.8)$$

These analytical estimates are included in Fig. 6 as blue dashed lines, showing an excellent agreement with the numerical solution. It should be noted that, with independence from the

distributor geometry, C_d approaches a constant value around $C_d = 0.61-0.64$ when $\Delta P_{\text{hole}} \gg \frac{1}{2}\rho v_{\text{dist}}^2$ [49]. A detailed comparison with experimental data is presented in [48], providing an estimate of $C_d = 0.63$ (that is adopted hereafter). Such pressure-dominated conditions are typical of capped distributors, and were verified for all our study cases. Similarly, the γ pre-factor is largely independent from the gas flow characteristics and, according to [48], weakly dependent on the geometry, and so the value is set to $\gamma = 0.71$. The least constrained coefficient, C_r , as well as the friction losses, are immaterial in the conditions discussed, as it is made clear through the analytic expressions in 3.5-3.7. The aforementioned values for the parameters γ and C_d are consistent with the CFD analysis of the control geometry displayed in Fig. 5.

flow [m ³ /h]	name	# holes	ΔL [mm]	D[mm]	d[mm]	$\overline{\Delta P_h}$ [mbar]	$\overline{v_h}$ [m/s]	θ_{max} [deg]
6.5	A	1	15	45	1	0.15	0.865	4.2
20	A	1	15	45	1	1.46	2.66	4.2
6.5	B	3	15	70	1	0.017	0.29	5.1
20	B	3	15	70	1	0.16	0.88	5.1
6.5	C	1	15	30	0.75	0.49	1.54	5.3
20	C	1	15	30	0.75	5.78	5.29	5.3
6.5	D	3	50	30	0.75	0.61	1.72	4.7
20	D	3	50	30	0.75	4.63	4.73	4.7

Table 2. Characteristics of the gas-distributor geometries discussed in this work. The first column indicates the gas flow (assumed to be Ar/CF₄ (99/1) at 10 bar and 25 °C). Columns 4-6 indicate the geometrical parameters of the distributor. Columns 7-9 indicate the average value of the pressure drop relative to the TPC, average discharge velocity, and maximum discharge angle of emission, respectively. Eight distributor rods of 5 m in length were considered in all cases, for the injection. Geometries A(single hole) and B(triple hole) are used as default for the CFD simulation, while geometries C(single hole) and D(triple hole) aim at illustrating that it is possible to reduce the diameter of the distributor rod, keeping a low value of the discharge angle. Column 3 indicates whether the perforation pattern is made out of individual holes or a triplet (one hole placed radially and the other two azimuthally).

In order to come to some plausible distributor geometries, the following design constraints were introduced: i) a diameter hole not much smaller than 1 mm, ii) a diameter of the distributor not much larger than 5 cm, iii) an inter-hole distance not larger than 5 cm, iv) a pressure drop below 10 mbar, v) a discharge velocity well below the speed of sound, and vi) a maximum discharge angle below or around 5°. Based on these requirements, the main challenge is to obtain a small discharge angle without neither letting the inter-hole distance and tube diameter grow too big, nor the hole diameter become too small. Four exemplary geometries satisfying the above conditions (*A-D*) are compiled in table 2, and we have focused in the remainder of the text on *A* (single hole) and *B* (triple hole). It might be argued that small distributor diameters like those given in *C* and *D* should be preferred. This can be in fact achieved for *A* and *B* as well, through minor adjustments of the geometry that have not been considered in the CFD simulations presented in this work. For instance, a reduction from a diameter of 7 cm to 3.5 cm in geometry *B* can be achieved by increasing the number of injection rods to 32 and increase the inter-hole distance to 60 mm, yet keeping the rest of the fluid properties as in table 2. Naturally, it is also possible to reduce the diameter to

3 cm or less and maintaining a small discharge angle through the increase in the thickness of the distributor walls, a study that falls outside the scope of this work. A slight preference towards geometries *A* and *B* stems from the fact that hole velocities above 1-2 m/s (as in *C*, *D*) showed a tendency to form large-scale vortices, that delay substantially the time for the impurities to achieve uniform mixing. Aiming at a comparative study, we opted for a design that guaranteed a range of velocities in the default distributor geometry (*B*) outside the region where the effect appears, for the gas flows studied. A CAD image of this geometry is shown in Fig. 7-a, whereas Fig. 7-b provides an equivalent geometry in terms of fluid parameters at the inlets, however with smaller-diameter distributors.

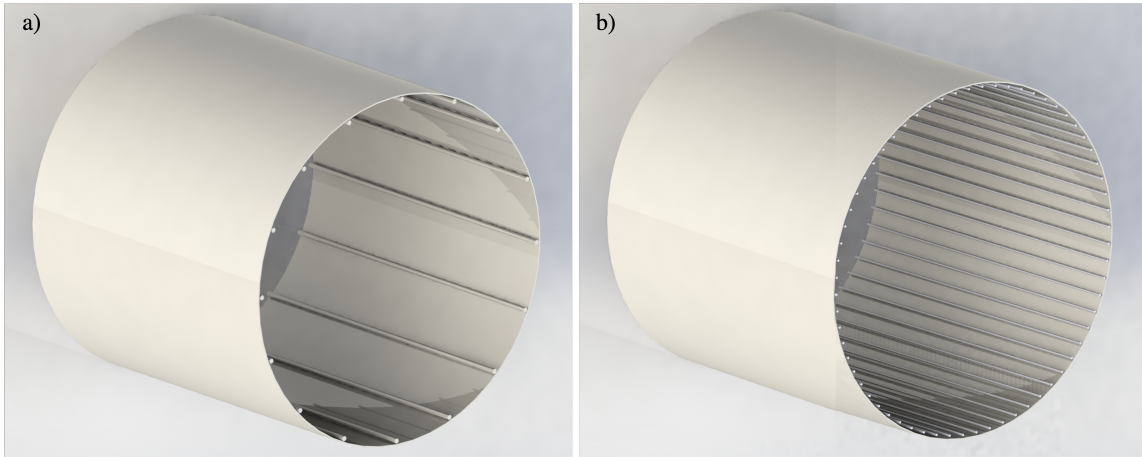


Figure 7. Left (a): gas distribution corresponding to geometry *B* in table 2, the default geometry studied in text. Right (b): modification of geometry *B*, employing $\times 4$ tubes with $\times 2$ smaller diameter, and holes separated $\times 4$, thus matching the same initial conditions of the fluid at the inlets.

3.2 CFD simulations

A numerical evaluation, based on the well established CFD methodology, allows for a realistic approach to describe the gas and impurity dynamics by calculating the velocity field in the overall volume of the field cage, including the injection setup. It is assumed that impurities, present in trace amount, do not modify the velocity field of the main gas. Translational invariance along the (axial) z dimension ($\frac{\partial}{\partial z} = 0$) was assumed. This choice clings on the (axial) orientation of the distributors and the discharge optimization performed in the previous section, that assures the discharge angle to be nearly perpendicular to the distributor (table 2). As discussed, the outgassing rate from the end-caps can be made sub-dominant relative to that from the field cage, approximately preserving the adopted symmetry. Although the region between holes cannot be well described in this approach, the distance chosen in geometries *A-D* in table 2 is sufficiently small (15-50 mm) to anticipate a negligible (local, at most) impact.

The hole aperture of the inlets and local pressure difference (distributor-TPC) were set to provide (simultaneously) the desired average velocity per hole and flow per unit length, based on the values in table 2. Achieving convergence in the simulations by setting the hole velocity instead of the pressure difference as an initial condition was not possible in general. The outlets were set to a fixed pressure of 10 bar. Gravity was included in simulation, and in particular the hydrostatic

pressure was added automatically at the inlets and outlets depending on their height. Outgassing was set perpendicular to the walls and to the distributors. As shown in Fig. 4, the mesh is finer closer to the holes and coarser towards the center of the field cage. To assure convergence, the solution was checked to be stable upon global up and down-scalings on the mesh size and variations on the time step.

The turbulent-flow ‘k- ε ’ model was selected, being adequate for simulating single-phase flows at high Reynolds numbers and suitable for incompressible or weakly compressible flows, and compressible flows at low Mach numbers. The ‘k- ε ’ model is the most validated turbulence model and performs well in confined flows where the Reynolds shear stresses are important. This model uses the Reynolds-averaged Navier-Stokes equations (RANS), introducing two more magnitudes: the turbulent energy (k) and the rate of turbulent energy loss (ε). These magnitudes have their corresponding differential equations coupling the velocity field (\vec{v}) with the viscous stress tensor \mathbf{K} (following COMSOL notation):

$$\rho \vec{\nabla} \cdot \vec{v} = 0, \quad (3.9)$$

$$\rho \frac{\partial \vec{v}}{\partial t} + \rho (\vec{v} \cdot \vec{\nabla}) \vec{v} = \vec{\nabla} \cdot [-P\mathbf{I} + \mathbf{K}] + \rho \vec{g}, \quad (3.10)$$

$$\rho \frac{\partial k}{\partial t} + \rho (\vec{v} \cdot \vec{\nabla}) k = \vec{\nabla} \cdot \left[\left(\mu + \frac{\mu_T}{\sigma_k} \right) + \vec{\nabla} k \right] + P_k - \rho \varepsilon, \quad (3.11)$$

$$\rho \frac{\partial \varepsilon}{\partial t} + \rho (\vec{v} \cdot \vec{\nabla}) \varepsilon = \vec{\nabla} \cdot \left[\left(\mu + \frac{\mu_T}{\sigma_\varepsilon} \right) + \vec{\nabla} \varepsilon \right] + C_{\varepsilon 1} \frac{\varepsilon}{k} P_k - C_{\varepsilon 2} \rho \frac{\varepsilon^2}{k}. \quad (3.12)$$

In the above expressions, 3.9 is the continuity equation for incompressible flow, \mathbf{I} is the identity matrix and \vec{g} is the gravity force. The following definitions are needed:

$$\mu_T = \rho C_\mu \frac{k^2}{\varepsilon}; \quad P_k = \mu_T \left[\vec{\nabla} \vec{v} : (\vec{\nabla} \vec{v} + (\vec{\nabla} \vec{v})^T) \right], \quad (3.13)$$

where μ_T is the turbulent viscosity (a correction to the viscosity μ because of the turbulent regime), P its pressure, and the inner product is defined as:

$$\mathbf{a} : \mathbf{b} = \sum_i \sum_j a_{ij} b_{ij}. \quad (3.14)$$

The dimensionless coefficients, called closure coefficients, of these equations are [47]:

$$C_{\varepsilon 1} = 1.44, \quad C_{\varepsilon 2} = 1.92, \quad C_\mu = 0.09, \quad \sigma_k = 1, \quad \sigma_\varepsilon = 1.3.$$

Finally, the transport of impurities (trace amount) is implemented based on Fick’s law:

$$\vec{J} = -D \vec{\nabla} c, \quad (3.15)$$

where \vec{J} is the particle flow per unit area and time, and c the impurity concentration in [L^{-3}]. This equation must be coupled to the continuity equation in presence of convection:

$$\frac{\partial c}{\partial t} + \vec{\nabla} \cdot \vec{J} + \vec{v} \cdot \vec{\nabla} c = 0, \quad (3.16)$$

and diffusion coefficients are taken from the last column in table 1. At the surface boundaries, the ‘no slip’ condition was used [50], as it is customary for solid boundaries and Newtonian fluids in macro-scale flow and non-rarefied conditions.

4 Results

4.1 TPC filling

A priori, the displacement of air during the chamber filling can be performed at flow rates higher than those imposed by the recirculation compressors, if need be. In the ideal case, it might even be possible to pump the TPC, although for large volumes this cannot be taken for granted. Here we consider for illustration the process of TPC filling at a flow rate of $6.5 \text{ m}^3/\text{h}$ ('typical' flow), in the default geometry (B). It has been assumed, for simplicity, that the chamber is filled quickly (and uniformly) up to 9 bar of Ar and 1 bar of air (by making use of the large pressure difference at the start of injection) and afterwards the flow of argon is set to the nominal one (that marks the time $t = 0 \text{ h}$ in simulation). In the absence of convection, the triple-hole distributor proposed in geometry B removes very efficiently the O_2 concentration from the region in between distributors and then the fresh argon gently displaces the Ar/ O_2 admixture upwards. The relatively low diffusion of O_2 at high pressure and its lower mass favors its extraction from the uppermost outlets.

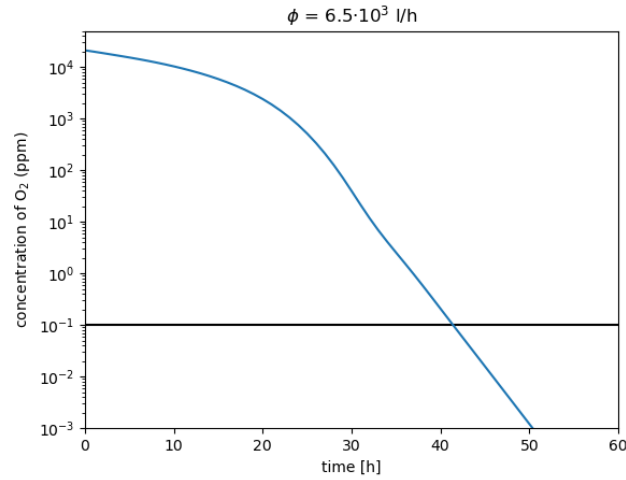


Figure 8. Evolution of the oxygen concentration upon starting the gas flow in the TPC ($\Phi = 6.5 \text{ m}^3/\text{h}$, $P = 10 \text{ bar}$), for distributor geometry B . The initial value corresponds to a 21% O_2 concentration and 1 bar of air / 9 bar of argon. The line shows the 0.1 ppm landmark, corresponding to a 10% charge loss in a cathode-anode electron transit.

Fig. 8 shows the concentration of oxygen integrated over the chamber as a function of time. It is worth noting that, in the limit of large diffusion (where O_2 would be uniformly distributed over the chamber at all times), the time constant for O_2 replacement would be directly $\tau_{\text{O}_2} = V/\Phi$ (see appendix), with V being the chamber volume (100 m^3). Reaching the 0.1 ppm landmark value, for instance, would take 188 h, about $\times 4.5$ more time than observed in the CFD simulations (42 h). While it is clear that convection currents due to power dissipation by active elements can slow down the displacement of oxygen in the final experimental conditions, it is safe to state that, in the absence of pumping, the filling time will be situated in the range 40-190 h. An alternative based on a modest increase of the gas flow during filling could be viable; however, a significant volume of gas will need to be disposed of, purified or recovered in real time.

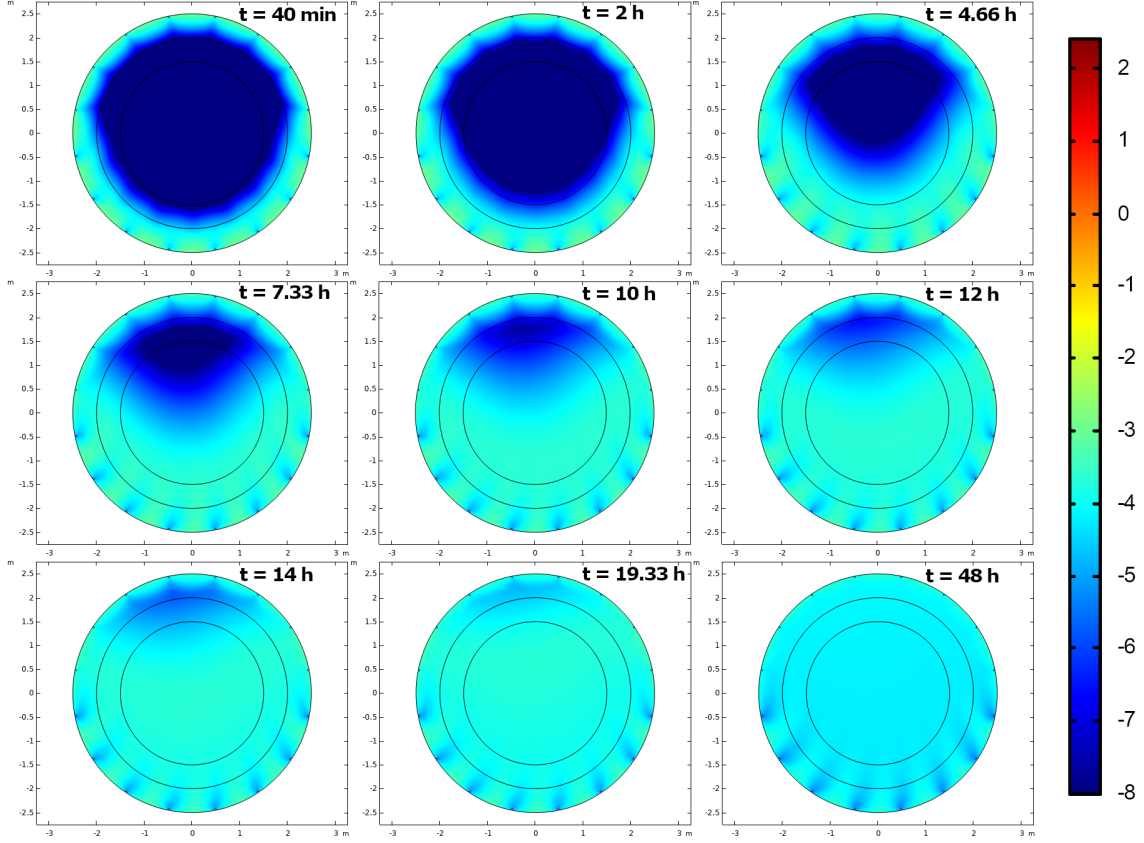


Figure 9. Time lapse of the distribution of O_2 concentration in our reference 10 bar Ar/ CF_4 TPC for geometry B (holes in ‘triplet’ configuration), under typical outgassing and flow rate conditions. The concentric circles mark the limits of the different mesh regions. The transient phase of the gas mixing can be observed mostly during the first 20 h. After that, the system approaches steady state and the concentration becomes homogeneous in the chamber. The images show clearly how the gas mixing is driven in these conditions by the velocity field, going from bottom to top. (The color bar displays the logarithm of the concentration in mol/m^3 .)

4.2 Oxygen contamination

When studying the evolution of oxygen, two outgassing rates have been considered: i) $Q = 10^{-8} \frac{\text{mbar}\cdot\text{l}}{\text{cm}^2\cdot\text{s}}$ (‘typical’) and ii) $Q = 0.05 \times 10^{-8} \frac{\text{mbar}\cdot\text{l}}{\text{cm}^2\cdot\text{s}}$ (‘optimistic’). Similarly, for the gas flow: i) $\Phi = 6.5 \text{ m}^3/\text{h}$ (‘typical’) and ii) $\Phi = 20 \text{ m}^3/\text{h}$ (‘optimistic’). The outgassing rate was assumed constant and equal to its value at 10 h. This has a dual benefit: i) it provides a safe upper limit to the O_2 concentration (compared to the anticipated $t^{-1/2}$ law) and ii) it allows a straightforward interpretation of the moment when the system achieves stationary conditions. Details are compiled in Table 1.

Fig. 9 shows the evolution of the O_2 concentration under typical outgassing and flow rate conditions for geometry B (triple-hole distributor). For comparison, Fig. 10 shows the results for geometry A (single-hole distributor) when the holes are radially-oriented. This latter case displays the formation of a vortex. Therefore, while in the default geometry B (hole triplet) the contaminants are uniformly mixed quickly thanks to the velocity field, in geometry A (hole singlet) the uniformity

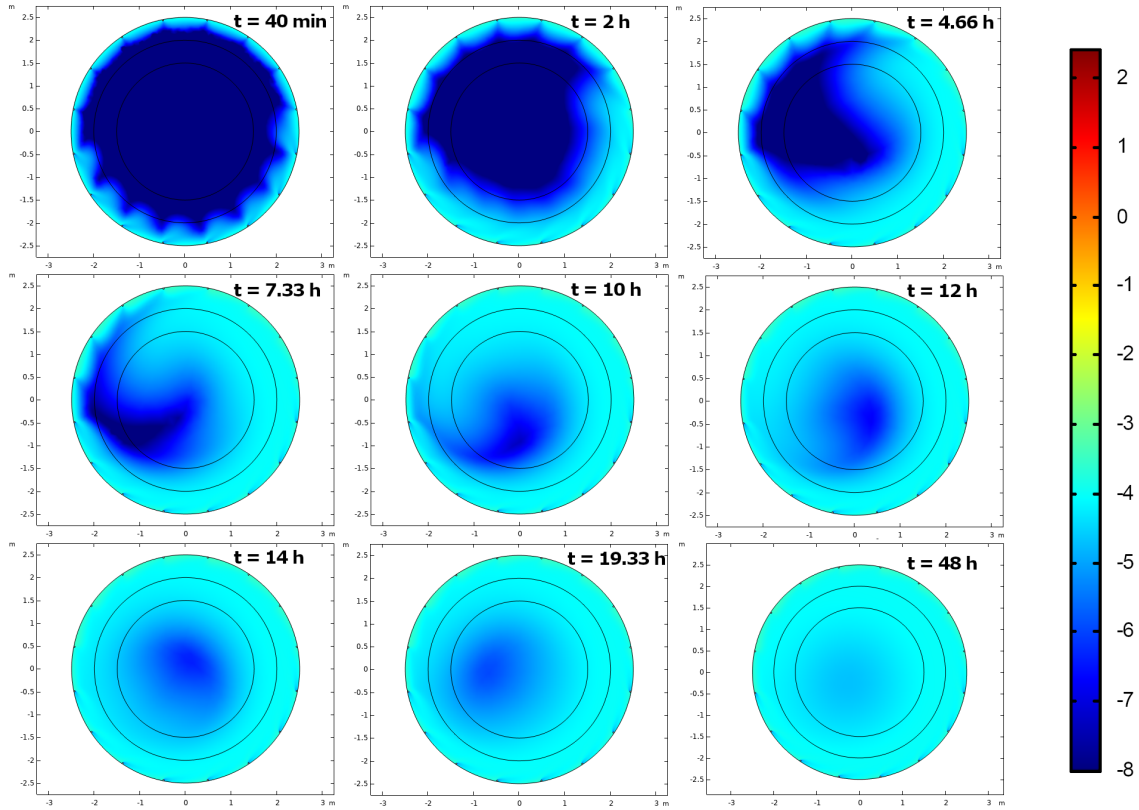


Figure 10. Time lapse of the distribution of O_2 concentration in our reference 10 bar Ar/CF_4 TPC for geometry A (radial holes), under typical outgassing and flow rate conditions. After 24 h, steady state conditions have not been achieved yet. (The color bar displays the logarithm of the concentration in mol/m^3 .)

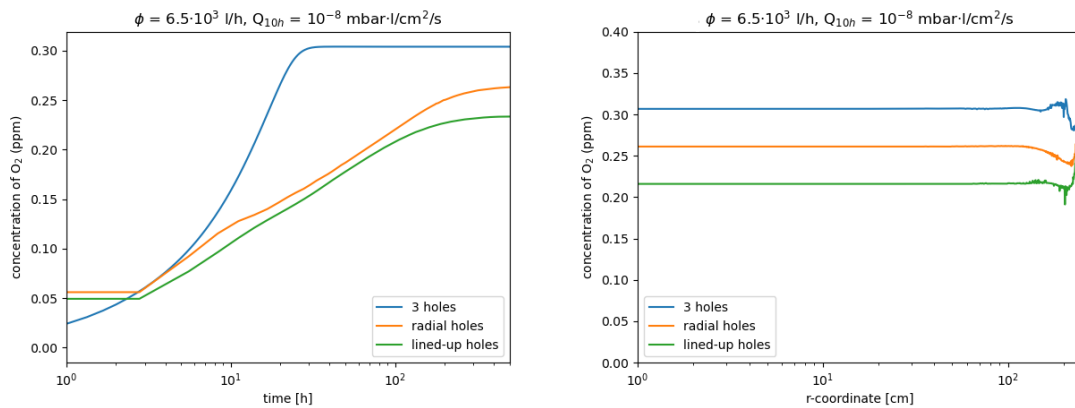


Figure 11. Oxygen concentration simulated up to 500 h in our reference 10 bar Ar/CF_4 TPC, under typical outgassing and flow rates, for three different distributor geometries (three holes: blue; single radial holes: orange; single lined-up holes: green). Left: evolution of the total O_2 concentration with time. Right: radial distribution (logarithmic X-scale) of O_2 at the 500 h mark, with all distributor geometries displaying a mostly homogeneous contaminant distribution. (The contribution from the outermost 5 cm of the chamber has been removed.)

is achieved through diffusion, involving considerably longer times. Single or double vortexes are prevalent in single-hole distributor geometries, for the conditions studied, but are absent in the triple-hole ones. The implications of this observation can be summarized in Fig. 11. In the left panel, the time evolution of the O₂ concentration is shown for three different distributor geometries (triple holes: blue; radial holes: orange; lined-up holes: green), corresponding to geometries *A* and *B* in table 2. The right panel shows the radial distribution of impurities (logarithmic X-scale) when all geometries have achieved steady state (500 h): it is completely homogeneous except in the outermost regions, where it can vary up to 30%. The triplet configuration reaches stationary conditions within 20 h, compared to almost $\times 10$ that time for the 1-hole geometries.³

It is difficult to assess the significance of the larger tendency to vortex formation in the single-hole distributors, and whether it will be maintained in an actual experiment when considering the exact geometry and the unavoidable convection currents stemming from temperature gradients. Notwithstanding, the triple-hole distributor is vortex-free and achieves consistently a faster mixing with contaminants as well as a more efficient sweeping of the outgassing from the chamber walls. This is illustrated in Fig. 12, where three different gas flows are compared under typical values of the outgassing rate (top figure: 2 m³/h, middle figure: 6.5 m³/h, bottom figure: 20 m³/h). The time evolution is displayed, up to 48 h, on the left column, while the radial distribution of contaminants is shown on the right column. Due to the low gas flow in the top figure (and correspondingly low discharge velocity), the time scale is too short to lead to vortex formation and the two distribution schemes perform similarly up to nearly the steady state value (1.4 ppm for these conditions). Even in the absence of vortex, the triple-hole distribution is more efficient at mixing due to a better sweeping of the chamber walls. For larger gas flows (middle and bottom figures), the fluid dynamics of the radial-hole geometry is dominated by the formation of a central vortex, with impurities reaching the central region through diffusion alone (right figures).

The results obtained in this section can be analyzed by comparison with the one-dimensional solutions, that effectively consider an ‘infinite diffusion’ scenario (see appendix). Fig. 13 shows how the observed time-dependence (red line) is reasonably well approximated by the 1-D solution (dashed line), implying that the achieved mixing rate is compatible with the ideal limit of perfect mixing. The blue line, obtained at $\times 20$ less outgassing (‘optimistic’ case) aims at illustrating that the curves obtained by CFD reflect a global scaling factor for different outgassing rates, following as well the expectation from the 1-D solutions (see appendix). The asymptotic value in Fig. 13 (red line) of 0.3 ppm would correspond to a 30% charge loss following the estimates in section 2.1. Considering the range of outgassing rates in table 1, an upper limit to the charge loss after 24 h can be situated in the range 1.5-30%, for the gas flow conditions in Fig. 2.1.

4.3 Water contamination

For Teflon, outgassing rates of water are far too high compared to O₂, so that if outgassing would not decrease over time then the necessary purity levels may never be achieved. Instead of assuming a

³The stationary limit following eq. C.3 in appendix is $\frac{Q \cdot A}{P \cdot \Phi} = 0.43$ ppm, to be compared with the simulated one of 0.31 ppm. The deviation can be attributed to i) the uncertainty in the flow estimate from the average velocity at the inlets and ii) the contribution from the last 5 cm of the chamber, that has a complex dynamics and has been removed here aiming at a simplified discussion (the last cm’s from the chamber are usually excluded from any physics analysis).

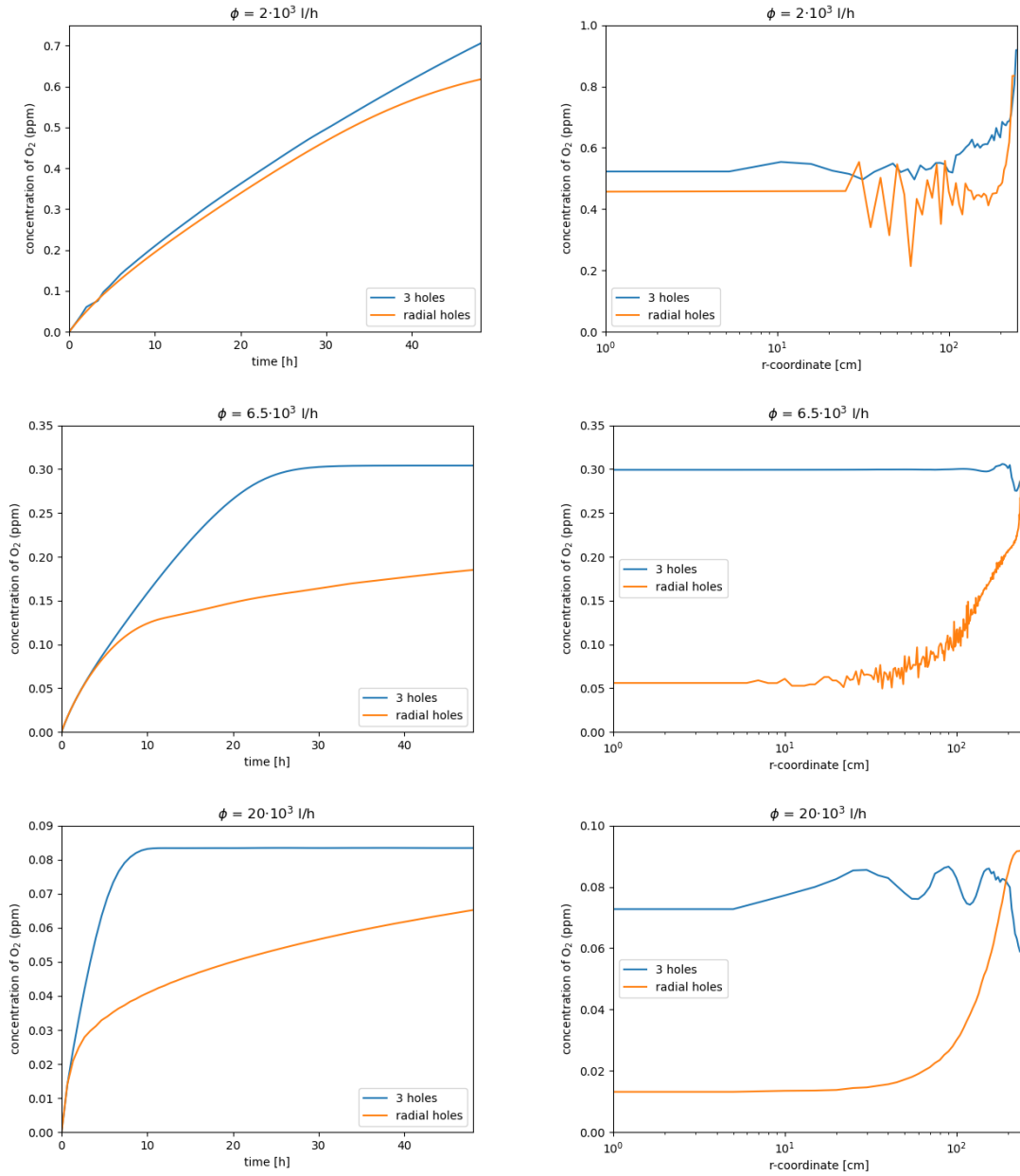


Figure 12. Time evolution of the O₂ contamination (left), and radial profile at the 48 h mark, in our reference 10 bar Ar/CF₄ TPC. Two distributor geometries are considered (triple-holes in blue, radial-holes in orange). From top to bottom, the gas flow is 2 m³/h, 6.5 m³/h and 20 m³/h, for a typical value of the outgassing rate. Steady state conditions for the triple-hole case are reached at about 70 h (top), 25 h (middle), and 8 h (bottom). Right: radial distributions reflecting, in the single-hole case, how impurities reach into the central region of the TPC mostly through diffusion from large radii. The wiggling radial pattern observed at high flow for the triple-hole case mirrors the position of the gas inlets. (The contribution from the outermost 5 cm of the chamber has been removed.)

constant value, we consider in this case the actual outgassing law based on eq. 2.7, with outgassing rates after 10 h taken from table 1: $3.5 \times 10^{-8} \frac{\text{mbar} \cdot \text{l}}{\text{cm}^2 \cdot \text{s}}$ ('optimistic') and $10 \times 10^{-8} \frac{\text{mbar} \cdot \text{l}}{\text{cm}^2 \cdot \text{s}}$ ('typical').

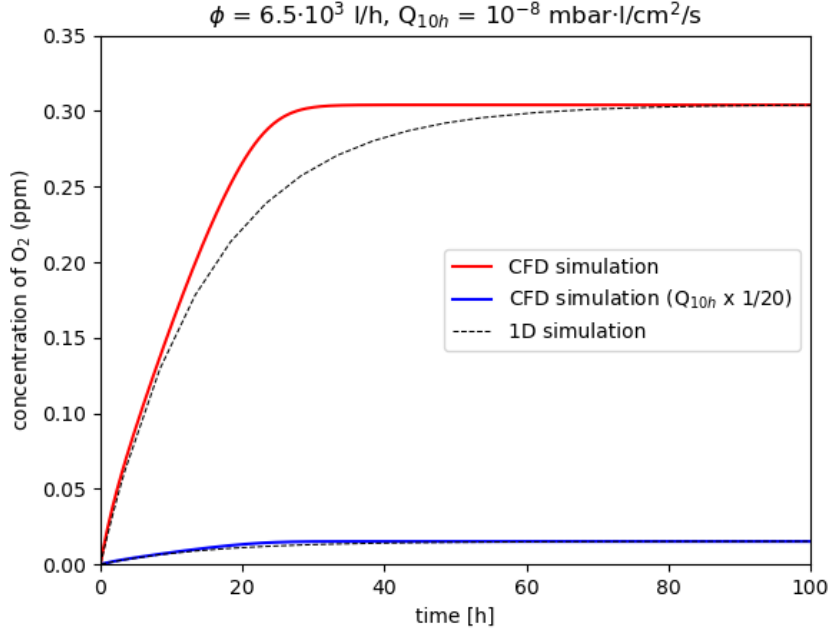


Figure 13. Time evolution of the O_2 contamination in our reference 10 bar Ar/CF₄ TPC for ‘typical’ outgassing and flow rates, in the default geometry B (holes in ‘triplet’ configuration) in red. A 1-D solution (‘infinite diffusion’ limit) is shown in dashed lines. The CFD solution for ‘optimistic’ outgassing values (blue) reflects a simple down-scaling, without altering the shape. (To account for the numerical deviation from the steady-state limit, as discuss earlier in text, the outgassing in the 1-D solution has been downscaled by 28%.)

We concentrate on the case of typical outgassing and flow rates, and five different Teflon thicknesses, including the case where Teflon would be so thick so as to preserve a $t^{-1/2}$ behaviour all the time throughout. Based on the analysis in the previous section, the configuration with triple-holes has been chosen. Results are shown in Fig. 14. For thicknesses below 10 mm, a transition between the $t^{-1/2}$ and exponential regimes can be observed. As the outgassing rates of H₂O are about 10 times larger than those of O₂ in case of Teflon, the time scales involved are larger too. The horizontal line shows the 1 ppm-level, that is a plausible requirement to keep space resolution undistorted below 1 mm, based on the analysis presented in section 2.1. For a thin-Teflon reflector down to 0.5 mm thickness, coupled to an ESR reflective coating (see e.g. [52]), that land-mark value is achieved in 46 h, while it reaches up to 99 h as the Teflon becomes thicker. The result is sobering: when considering the displacement of air during filling and the time needed for water (oxygen) to fall below the concentration that makes its contribution negligible for tracking (attachment), about 6-10 days time would be typically needed. Well-defined cleaning protocols and surface treatment, as discussed for example in [37], together with an increase of the gas flow above the levels discussed here, or designing the system in compliance with the requirements needed for pumping, could plausibly reduce these times to the scale of about 1-2 days. On the other hand, additional (uncontrolled) outgassing sources would render the operation of the detector problematic.

Additional studies are presented in Fig. 15 in order to illustrate the main dependencies. On

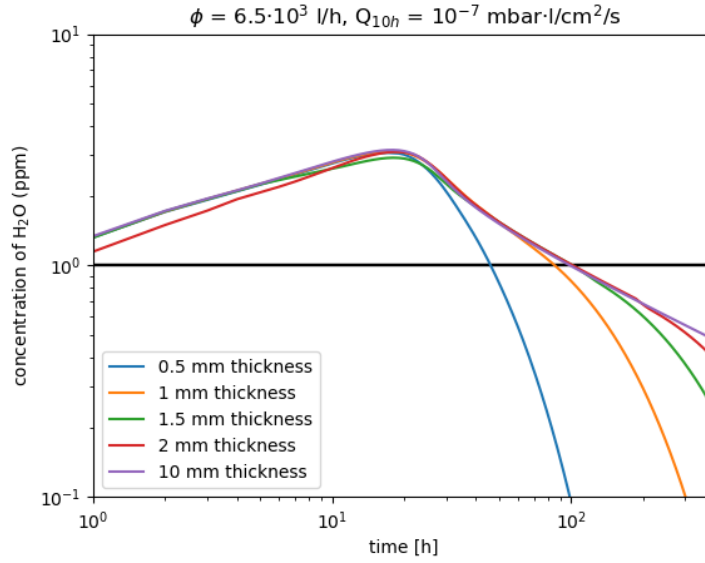


Figure 14. Evolution of water concentration as a function of time for ‘typical’ values of the outgassing and flow rates, in our reference 10 bar Ar/CF₄ TPC, for geometry *B* (triple-hole distributor). Three different Teflon thicknesses are considered. The land-mark value of 1 ppm (less than 1 mm track distortion on a 5 m drift) is achieved at 99 h in the worse-case scenario.

the left-figure, the behaviour for different gases is shown for a fixed flow rate of 6.5 m³/h (argon: continuous lines; xenon: dashed lines). It can be seen how, despite the diffusion coefficient of H₂O being slightly larger in argon by about 50% (table 1), the impact on the time-evolution of the impurities is almost indiscernible. When reducing the pressure down to 1 bar, the $\times 10$ increase in the diffusion coefficient accelerates the mixing as expected, however the reduction in the position of the maximum is a mere 30%. As the number of normal liters is accordingly reduced by a factor $\times 10$ in those conditions, the concentration of impurities increases in inverse proportion (the Ar and Xe lines at 1 bar have been downscaled by $\times 10$).

Fig. 15-right shows a comparison with the 1-D solutions for the case of time-dependent outgassing (see appendix). As for the case of constant outgassing, the results compare well with the 1-D model, despite the agreement is qualitatively worse. Artificially increasing the gas diffusion accelerates the mixing, but very mildly in the conditions studied (as indirectly shown in Fig. 15-left). The conclusion is once again that the velocity field in combination with gas diffusion can distribute the outgassed species uniformly over the chamber for the optimized ‘triplet’ distributor, as seen in Fig. 9. Also in this case, simulations for lower (‘optimistic’) outgassing rates display an exact down-scaling compared to the solutions presented in Fig. 15, as expected from the 1-D solutions.

4.4 Nitrogen contamination

Nitrogen can be removed from the system by flushing the main gas through ‘hot’ (temperature-activated) purifiers/getters, a common asset for the operation of noble gas detectors. The process of nitrogen purification becomes challenging, however, in case of operation under large gas flows

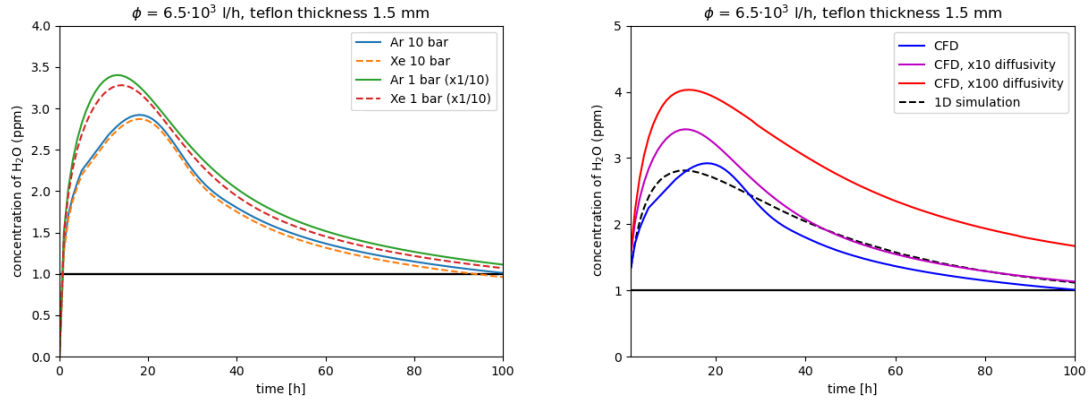


Figure 15. Left: water concentration as a function of time for ‘typical’ values of the outgassing and flow rates, in our reference 10 bar Ar/CF₄ TPC, assuming a Teflon thickness of 1.5 mm. Different gas species (Ar: continuous; Xe: dashed) and pressures have been considered. Right: time-dependence for Ar/CF₄ at 10 bar (blue) and comparison with results assuming an artificially increased diffusion coefficient of $\times 10$ (purple) and $\times 100$ (red). Dashed-lines correspond to a 1-D model (‘infinite diffusion’ limit).

(that could modify the getter temperature) and/or in the presence of molecular additives such as CF₄ (that may react with the getter materials). Following conventional wisdom, and as long as a purification system compatible with Ar/CF₄ operation is not demonstrated at the necessary scale, we will assume conservatively that N₂ accumulates in the TPC as time passes.

Fortunately, the tolerance to N₂ is by far the largest of common outgassing species, up to 10 ppms (table 1). Based on the the time profile of the outgassing rate (eq. 2.7), the range of outgassing values in table 1, and the chamber volume, the evolution of N₂ inside the TPC can be approximated as (see appendix):

$$f_{N_2} \sim (3 - 9)\text{ppms} \cdot \sqrt{t[\text{days}]} \quad (4.1)$$

with the pre-factor covering the range dubbed earlier as ‘optimistic’ (3 ppm) and ‘typical’ (9 ppm). In practice, this expression indicates that N₂ can approach harmful concentrations pretty quickly, within one day, however the concentration will increase slowly thereafter. Assuming 10 years of continuous operation, N₂ concentration would approach 180-540 ppms by the end of the experiment. In the absence of purification, the equivalent of 18-54 ND-GAr volumes of fresh gas would need to be added during the detector live time, to keep the N₂ concentration within bounds. Such an estimate represents an upper limit since: i) the outgassing rate of plastics is expected to fall exponentially as the material becomes N₂-depleted (eq. 2.7), and ii) the impact of N₂ contamination on the tracking capabilities might be correctable with adequate calibration systems. On the other hand, as discussed earlier, these concentrations are unlikely to create problems for the optical signal.

There are several ways to address the most convenient commissioning strategy, for which a reliable experimental estimate of the N₂ outgassing rates would be essential, first and foremost. As an example, the system could be operated in pure argon gas with both hot and cold getters for about 10 days, prior to CF₄ injection. N₂ concentration would then reach back to 10 ppms in another 10 days for ‘typical’ outgassing values, and 30 days for ‘optimistic’ estimates (eq. 4.1). Injection of fresh gas in the range 0.3-1% after the first 10 days would guarantee operation around or below the

10 ppm N₂ landmark. In the presence of calibration systems, on the other hand, that would allow to correct track distortions as large as 1 cm (100 ppm of N₂), few additional ND-GAr volumes, in the range 2-6, would be needed.

As CF₄ has a very high GWP, it seems unavoidable that ‘old’ gas needs to be cryorecovered and CF₄ distilled prior to disposal to the atmosphere, while fresh gas is being injected.

5 Summary and conclusions

In this work we have addressed the problem of gas distribution and impurity mitigation for next-generation Time Projection Chambers in the fields of Neutrino Physics and Rare Event Searches. Specifically, we focused on the performance of an Ar/CF₄ (99/1) optical TPC of 5 m-length/5 m-diameter at 10 bar, with a field cage covered with Teflon lining, as recently suggested in [14]. We have considered an axial gas distribution scheme (along the electric field direction), that is more independent from the specific end-cap design as well as more easily tractable through computational fluid dynamics (CFD) simulations.

Distributor rods are modeled through a combined approach based on CFD simulations and generalized continuity equations, that allow a straightforward optimization. The approach allows to show that, for the flow rates of relevance to next-generation TPCs, a nearly-perpendicular discharge angle (less than 5° with respect to the normal) can be achieved for hole diameters at the mm-diameter scale, thus ensuring a priori a good bottom-up circulation of the gas for any position along the axial direction, without the creation of gas pockets. Holes are separated by 10-50 mm, the rod diameters being in the range 30-70 mm (possibilities for further reducing this diameter are given in text, although they are outside the scope of this work). The discharge velocity of the holes and the pressure drop at the distributor rod are generally far from the regime where they could pose problems, and are not critical in the optimization.

The proposed gas distribution, based on eight perforated plastic rods (capped at their ends) for injection and eight for extraction, can efficiently sweep the outgassing from the walls when a triple-hole perforation is implemented (one hole situated along the radial direction and two azimuthally). By contrast, single-hole distributors perform worse at sweeping the gas from the walls and are more prone to vortex formation, resulting in much longer times to achieve steady-state conditions. Additionally, the triple-hole configuration leads to an efficient displacement of air during chamber filling (down to 0.1 ppm of O₂) in about 42 h time, that is ×4.5 faster than expected from a diffusion-dominated 1-D model. (Assuming no pocket formation, the 1-D model provides an estimate of the longest extraction time).

The contamination of O₂ (H₂O) during chamber operation was studied, assuming circulation in closed loop with the gas forced into conventional ‘cold’ getters. For a realistic flow rate of 6.5 m³/h at 10 bar, a maximum impurity level of 0.3 ppm (3 ppm) would be achieved in a bit over 24 h for typical values of the outgassing rates ($Q_{10h} \simeq 10^{-8} \frac{\text{mbar}\cdot\text{l}}{\text{cm}^2\cdot\text{s}}$ for O₂, and $Q_{10h} \simeq 10^{-7} \frac{\text{mbar}\cdot\text{l}}{\text{cm}^2\cdot\text{s}}$ for H₂O). These concentrations translate into maximum charge losses of about 30% (due to O₂) and track distortions of 3 mm (due to H₂O). The deterioration in the TPC response is reduced by a factor of 3 after 100 h, approximately following the anticipated reduction of the outgassing rate for technical plastics, as $\sim t^{-1/2}$. Generally speaking, and based on our experimental survey of the Teflon outgassing rates, after 100 h the expected losses due to attachment would be situated in the range 0.5% (‘optimistic’)-10% (‘typical’), with track distortions ranging between 0.3 mm (‘optimistic’) and

1 mm(‘typical’). In the proposed gas distribution scheme, for both O₂ and H₂O, mixing with the main TPC gas takes place at a pace compatible with the expectation from a diffusion-dominated 1-D model, that provides a benchmark for the shortest mixing time achievable in practice. Importantly, this close-to-ideal mixing renders an uniform distribution of contaminants within merely 24 h, a relevant feature in the need of applying corrections to reconstructed events.

Under the conservative assumption that N₂ purification at high flows and in the presence of CF₄ needs of dedicated studies and cannot be taken for granted at the moment, we discussed mitigation strategies to the problem of N₂ accumulation. It is shown that a total of fresh gas worth 18(‘optimistic’)/54(‘typical’) TPC volumes would be needed during 10 years of continuous operation, a requirement that can be met for instance by injecting fresh gas at a mere 0.3-1% fraction of the flow of the main gas line. If track distortions of up to 1 cm (100 ppm of N₂) could be corrected online through (laser-based or other similar) calibration systems, the additional fresh gas will be situated in the range of 2(‘optimistic’)-6(‘typical’) additional TPC volumes. These values are comparable to the ones needed during chamber filling, if TPC pumping would not be possible.

The above discussion, as well as most of the work on the body of the paper, focus on ‘typical’ values of the outgassing and gas flow rates, but there is room for improvement, and lower outgassing values might be achieved through suitable cleaning/surface finish protocols, while higher gas flows will likely become affordable in a few-year time scale. Ultimately this work is aimed at showing that, while operation of the optical TPC discussed here seems perfectly viable from the point of view of material compatibility, detailed outgassing assays of the materials involved in construction seem crucial to ensure the chamber performance and the necessary mitigation strategies.

Acknowledgments

This research has been funded by the Spanish Ministry (‘Proyectos de Generación de Conocimiento’, PID2021-125028OB-C21, PID2021-125028OB-C22). It has also received complementary financial support from the regional government Xunta de Galicia (Centro singular de investigación de Galicia accreditation 2019-2022), and by the national program “María de Maeztu” (Units of Excellence program MDM-2016-0692). We thank CERN for computing resources.

References

- [1] F. Sauli, *Gaseous Radiation Detectors*, Cambridge University Press, 2014.
- [2] D.R. Nygren, *The Time Projection Chamber: A new 4 π detector for charged particles*, Tech. Rep. PEP-144 (1974).
- [3] J. Hilke, *Time projection chambers*, Rept. Prog. Phys. 73 (2010) 116201.
- [4] D. González-Díaz, F. Monrabal and S. Murphy, *Gaseous and dual-phase time projection chambers for imaging rare processes*, Nucl. Instrum. Meth. A 878 (2018) 200.
- [5] A. Abed Abud et al (DUNE collaboration), *A Gaseous Argon-Based Near Detector to Enhance the Physics Capabilities of DUNE*, Contribution to: Snowmass 2021 • e-Print: 2203.06281 [hep-ex].
- [6] A. Abed Abud et al (DUNE collaboration), *DUNE Phase-II: Scientific Opportunities, Detector Concepts, Technological Solutions*, accepted in JINST.
- [7] C. Adams et al. (NEXT collaboration), *Sensitivity of a tonne-scale NEXT detector for neutrinoless double-beta decay searches*, JHEP08(2021)164.

- [8] S. E. Vahsen et al *CYGNUS: Feasibility of a nuclear recoil observatory with directional sensitivity to dark matter and neutrinos*, preprint arXiv:2008.12587.
- [9] <https://www.epa.gov/ghgemissions/understanding-global-warming-potentials>, last accessed 22-12-2024.
- [10] M. Huk et al., *Electron attachment to oxygen, water and methanol, in various drift chamber gas mixtures*, Nucl. Instr. Meth. A, 267(1988)107.
- [11] *ALICE Technical Design Report of the Time Projection Chamber*, CERN/LHCC 2000–001 ALICE TDR 7 (2000).
- [12] S. Rossegger, *Simulation & Calibration of the ALICE TPC including innovative Space Charge Calculations*, CERN-THESIS-2009-124.
- [13] A. Zhang et al., ‘Modeling impurity concentrations in liquid argon detectors’, Nucl. Instr. Meth. A 1010(2021)165491.
- [14] A. Saá-Hernández et al., *On the determination of the interaction time of GeV neutrinos in large argon gas TPCs*, submitted to EPJC, preprint: arXiv:2401.09920.
- [15] P. Amedo et al., *Primary scintillation yields induced by α particles in gas mixtures of Argon/CF₄ at 9.5 bar*, submitted to EPJC, arXiv:2410.17853.
- [16] P. Amedo et al., *Observation of strong wavelength-shifting in the argon-tetrafluoromethane system*, Front. Detect. Sci. Technol, 10.3389/fdest.2023.1282854.
- [17] P. Amedo et al., *Scintillation of Ar/CF₄ mixtures: glass-THGEM characterization with 1% CF₄ at 1–1.5 bar*, JINST 19 (2024) 05, C05001.
- [18] A. Andronic et al., *Pulse height measurements and electron attachment in drift chambers operated with Xe, CO₂ mixtures*, Nucl. Instr. Meth. A, 498,1-3(2003)143.
- [19] G. Thieme et al., *Mass Spectrometer Investigation of Gas Emission from Plastics*, Vacuum, 13, 4(1963)137.
- [20] F. Bloch and N. E. Bradbury, *On the Mechanism of Unimolecular Electron Capture*, Phys. Rev. 48 (1935) 689.
- [21] A. Herzenberg, *Attachment of Slow Electrons to Oxygen Molecules*, J. Chem. Phys. 51 (1969) 4942.
- [22] B. Al Atoum, S. F. Biagi et al., *Electron transport in gaseous detectors with a Python-based Monte Carlo simulation code*, Comp. Phys. Comm. 254(2020)107357.
- [23] L. Rogers et al., *High voltage insulation and gas absorption of polymers in high pressure argon and xenon gases*, JINST 13(2018) P10002.
- [24] G. Renault et al., *The laser of the ALICE Time Projection Chamber*, Int. J. of Mod. Phys. E, 7-8(2007)2413.
- [25] G. Martínez Lema et al. (NEXT collaboration), *Calibration of the NEXT-White detector using 83mKr decays*, JINST 13(2018)P10014.
- [26] P. Hamacher-Baumann et al., *A gas monitoring chamber for high pressure applications*, JINST 16(2021)P08030.
- [27] R. Santorelli et al., *Spectroscopic analysis of the gaseous argon scintillation with a wavelength sensitive particle detector*, Eur. Phys. J. (2021) 81:622.

- [28] H. Keller-Rudek, G. K. Moortgat, R. Sander, and R. Sörensen, *The MPI-Mainz UV/VIS spectral atlas of gaseous molecules of atmospheric interest*, Earth Syst. Sci. Data, 5, 365–373, (2013), <https://www.uv-vis-spectral-atlas-mainz.org/uvvis/> (last accessed 11-08-2024).
- [29] T. Takahashi, *Emission spectra from Ar-Xe, Ar-Kr, Ar-N₂, Ar-CH₄, Ar-CO₂ and Xe-N₂ gas scintillation proportional counters*, Nucl. Instr. Meth. 205 (1983) 591.
- [30] C. D. R. Azevedo et al., *Microscopic simulation of xenon-based optical TPCs in the presence of molecular additives*, Nucl. Instr. Meth. A 877(2018)157.
- [31] A. Pansky, et al. *The scintillation of CF₄ and its relevance to detection science*, Nuclear Inst. and Methods A 354(2–3)(1995),262.
- [32] L. M. S. Margato, et al. *Effect of the gas contamination on CF₄ primary and secondary scintillation*, Nucl. Instr. Meth. A, 695(2012)425.
- [33] B. J. Mount et al (LUX collaboration), *LUX-ZEPLIN (LZ) Technical Design Report*, Preprint: arXiv:1703.09144.
- [34] V. Álvarez et al. (NEXT collaboration), *NEXT-100 Technical Design Report (TDR). Executive summary*, JINST 7(2012)T06001.
- [35] K. Jousten, *Sorption and Diffusion*, in Handbook of Vacuum Technology, Wiley-VCH Verlag GmbH & Co. KGaA, 2016.
- [36] S. G. Sammartano et al., *Outgassing rates of PEEK, Kapton and Vespel foils*, CERN-ACC-NOTE-2020-0039.
- [37] K. F. Poole, M. M. Michaelis, *Hialvac and Teflon outgassing under ultra-high vacuum conditions*, Vacuum, 30, 10(1980)415.
- [38] R. Grinham, A. Chew, *A review of outgassing and methods for its reduction*, Appl. Sci. Conver. Technol. 26(5):95-109(2017).
- [39] S. Joshi, *Outgassing studies on thermal control coatings for micro-satellites*, Aircraft Engineering and Aerospace Technology, 83, 2(2011)69.
- [40] Ari Riihimäki, *Outgassing Studies of Some Accelerator Materials*, CERN-THESIS-2019-061.
- [41] Aalseth, C. E., Abdelhakim, S., Acerbi, F., Agnes, P., Ajaj, R., Albuquerque, I., et al. *Design and construction of a new detector to measure ultra-low radioactive isotope contamination of argon*. JINST 15 (2020) P02024. doi:10.1088/1748-0221/15/02/p02024
- [42] Adam John Lowe, et al., *ARIADNE+: Large Scale Demonstration of Fast Optical Readout for Dual-Phase LArTPCs at the CERN Neutrino Platform*, Phys. Sci. Forum 2023, 8(1), 46.
- [43] E. N. Fuller et al., *Diffusion of Halogenated Hydrocarbons in Helium. The Effect of Structure on Collision Cross Sections*. The Journal of Physical Chemistry, Vol 73, number 11.
- [44] R. C. Reid, J. M. Prausnitz, B. E. Poling, et al., *The properties of gases and liquids*, 4th edition. McGraw-Hill.
- [45] Francesc Monrabal, Marc Querol (NEXT), private communication.
- [46] <https://www.comsol.com/release/5.5>, last accessed 18-10-2024.
- [47] B.E. Launder, A. Morse, W. Rodi and D.B. Spalding, *The prediction of free shear flows - A comparison of the performance of six turbulence models*, Proceedings of NASA Conference on Free Shear Flows, Langley (1972). Also, Imperial College Mechanical Engineering Department Report TM/TN/A/19.

- [48] B. J. Bailey, *Fluid flow in perforated pipes*, Journal Mechanical Engineering Science (1975).
- [49] Van Der Hegge Zijnen, B. G. *Flow through uniformly tapped pipes*, Appl. Sci. Res. 1951 A3, 144-162.
- [50] M. D. Deshpande et al., *The No-Slip Boundary Condition in Fluid Mechanics*, pg 61-71.
- [51] B. Asamoah et al., *Identification of Plastic Type and Surface Roughness of Film-Type Plastics in Water Using Kramers–Kronig Analysis*, Chemosensors 2020, 8(4), 88.
- [52] J. Haefner et al, *Reflectance and fluorescence characteristics of PTFE coated with TPB at visible, UV, and VUV as a function of thickness*, JINST 18 (2023) P03016.

A Iterative implementation of a multi-hole distributor

The mass and momentum -balance equations for each hole section (eqs. 3.1 and 3.2) can be solved iteratively: for an assumed gas flow (velocity) at the entrance of the distributor, the pressure upstream of the first hole is scanned till the velocity downstream of the last hole converges to zero (Fig. 16). The set of hole-equations that need to be iteratively propagated along the distributor is:

$$\frac{P_i + P_{i+1}}{2} = P_{\text{TPC}} + \frac{\rho D^4 (v_i - v_{i+1})^2}{2d^4 C_{d,i}^2}, \quad (\text{A.1})$$

$$P_{i+1} - P_i = C_{r,i} \frac{1}{2} \rho (v_i^2 - v_{i+1}^2). \quad (\text{A.2})$$

C_d , C_r are dependent on the gas properties and little-dependent on geometry. We adopted the formalism in [48], in which C_d is parameterized as a function of the ratio $\frac{1}{2} \rho v_{\text{up}}^2 / \Delta P_{\text{hole}}$ and C_r as a function of $\Delta v = v_{\text{up}} - v_{\text{down}}$.

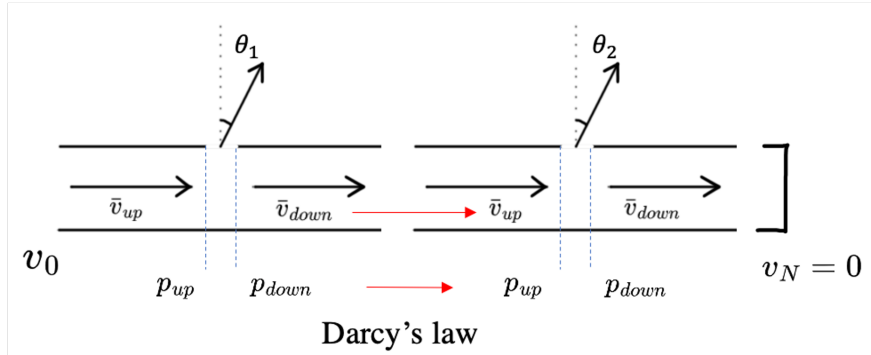


Figure 16. Perforated gas distributor capped at its end, together with the main magnitudes introduced in text. The sketch also gives an approximate representation of the solving method, that tries an initial value P_{up} upstream of the first hole, for an assumed flow, and iterates until a null velocity is obtained at the end of the distributor.

For a complete description, equations A.1-A.2 must be coupled hole-by-hole after accounting for any loss due to friction. The pressure drop in between hole sections is included through Darcy's friction law:

$$P_{\text{up}(i+1)} - P_{\text{down}(i)} = f_D \frac{\Delta L}{D} \rho \frac{v_{\text{down}(i)}^2}{2}, \quad (\text{A.3})$$

where ΔL is the distance between holes, ρ the gas density and f_D is Darcy's friction coefficient. A distinction is made, as customary, between laminar ($Re < 4000$) and turbulent ($Re > 4000$) regime,

with Re being the Reynolds number:

$$Re = v_{\text{down}(i)} \cdot \Delta L \cdot \frac{\rho}{\mu}, \quad (\text{A.4})$$

and μ is the (dynamic) viscosity of the fluid. For laminar flow $f_D = 64/Re$ is assumed and, for turbulent flow:

$$\frac{1}{\sqrt{f_D}} = -2 \log \left(\frac{k_s}{3.7D} + \frac{2.51}{Re \cdot \sqrt{f_D}} \right).$$

Here k_s is the roughness of the pipe wall (a typical value for a generic acrylic material was assumed: $k_s = 1.1 \mu\text{m}$ [51]).

B Useful analytic limits for capped distributors

The solution to v_d , for an initial upstream velocity v_u , can be easily obtained from eqs. 3.1 and 3.2:

$$v_d = \frac{\frac{D^4}{d^4} \frac{1}{C_d^2} \rho v_u - \sqrt{\frac{1}{4} C_r^2 \rho^2 v_u^2 + 4 \left(\frac{1}{2} \frac{D^4}{d^4} \frac{1}{C_d^2} \rho + \frac{1}{4} C_r \rho \right) (P_u - P_{\text{TPC}})}}{2 \left(\frac{1}{2} \frac{D^4}{d^4} \frac{1}{C_d^2} \rho + \frac{1}{4} C_r \rho \right)}. \quad (\text{B.1})$$

Since C_r is bound to $[0, 2]$ and C_d to $[0, 1]$ it follows that:

$$\frac{1}{4} C_r \ll \frac{1}{2} \frac{D^4}{d^4} \frac{1}{C_d^2}, \quad (\text{B.2})$$

as long as $d < D$, that is fulfilled in the distributor proposed in text by at least one order of magnitude. This allows neglecting the right-term in both the numerator and denominator of eq. B.1. The left-term inside the square root is very small, part through the above relation, part because:

$$\frac{1}{2} \rho v_u^2 \ll P_u - P_{\text{TPC}}. \quad (\text{B.3})$$

This is typical of a capped distributor. It has been verified during simulations that the pressure difference always exceeds the velocity term by at least a factor of 10, and generally much more. Finally, friction losses from eq. A.3 are very small due to the smallness of the ratio $\Delta L/D$ in the cases discussed (generally, 10% at most), so we may disregard the effect too.

It therefore follows, from the above considerations, that:

$$P_u - P_{\text{TPC}} \simeq \Delta P_{\text{hole}} \simeq \frac{1}{2} \frac{D^4}{d^4} \frac{1}{C_d^2} \rho (v_d - v_u)^2, \quad (\text{B.4})$$

irrespective from the hole position. If we assume that the discharge is uniform for each hole, that is observed in present conditions to better than 5%, then it also follows from mass balance that:

$$(v_d - v_u) \cdot \pi \left(\frac{D}{2} \right)^2 = \Phi_{\text{hole}} = v_{\text{hole}} \cdot \pi \left(\frac{d}{2} \right)^2. \quad (\text{B.5})$$

Under the assumption of uniform discharge, the flow per hole relates to the total flow as $\Phi_{\text{hole}} = \Phi/N_{\text{holes}}$. The analytic expressions given in eq. 3.5, 3.6 can be finally obtained:

$$\Delta P_{\text{hole}} \simeq \frac{1}{2} \frac{1}{C_d^2} \rho v_{\text{hole}}^2, \quad (\text{B.6})$$

$$v_{\text{hole}} \simeq \frac{\Phi}{\text{total hole area (t.h.a.)}}. \quad (\text{B.7})$$

Although C_d is fluid-dependent, in the pressure-dominated regime defined by eq. B.3 it approaches the asymptotic limit discussed in text: $C_d \simeq 0.63$.

The discharge angle can be finally evaluated from expression:

$$\theta = \gamma \cdot \arctan \left(\sqrt{\frac{\frac{1}{2} \rho v_u^2}{\Delta P_{\text{hole}}}} \right). \quad (\text{B.8})$$

The maximum discharge angle corresponds to the first hole upstream, for which:

$$v_u = \frac{\Phi}{N_{\text{pipes}}} \frac{1}{\pi (D/2)^2}, \quad (\text{B.9})$$

and substituting the expression obtained previously for ΔP_{hole} in the limit of small angles, we arrive at expression 3.7 in text:

$$\theta_{\text{max}} \simeq \gamma C_d \frac{d^2}{D^2} \frac{L_{\text{dist}}}{\Delta L}. \quad (\text{B.10})$$

As γ is weakly dependent on the fluid properties and geometry (e.g. [48]), a value of $\gamma = 0.71$ has been assumed.

The analytical expressions presented here for ΔP_{hole} , v_{hole} and θ_{max} have been found to agree with the exact numerical treatment to better than a few % for all the conditions discussed in this work. This has been illustrated for instance in Fig. 6.

C Time-dependent differential equations

In an idealized situation, we can model the outgassing and cleaning in the control volume as a simple mass balance, as in the scheme shown in Fig. 17. In this case, the flow of contaminants (X) can be represented as

$$\frac{dN_X}{dt} = q(t) - \frac{dN_{\text{Ar}}}{dt} \cdot \frac{N_X}{N_{\text{Ar}}}, \quad (\text{C.1})$$

where $q(t)$ represents the supply of contaminants (outgassing rate, in this case in units of number of molecules per unit time), $\frac{dN_{\text{Ar}}}{dt}$ is the flow rate of Ar (in this case in units of number of atoms per unit time), and $\frac{N_X}{N_{\text{Ar}}}$ is the probability that a molecule X exits the control volume (is ‘cleaned’) at a given time. This assumption is referred in text as the ‘diffusion-dominated limit’, under which new molecules of type X are distributed over the control volume instantly.

C.1 Constant outgassing rate

To solve the previous differential equation, we first consider the case where the outgassing rate $q(t)$ is constant over time. Under this assumption, we can easily integrate equation (C.1) obtaining

$$N_X(t) = \frac{q}{\frac{1}{N_{\text{Ar}}} \frac{dN_{\text{Ar}}}{dt}} \left(1 - \exp \left\{ -\frac{1}{N_{\text{Ar}}} \frac{dN_{\text{Ar}}}{dt} \cdot t \right\} \right), \quad (\text{C.2})$$

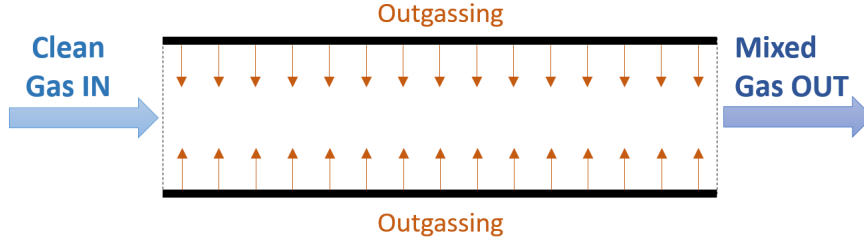


Figure 17. Schematic representation of the 1-D model used in text.

once we consider that the concentration of contaminants is 0 at $t = 0$.

If the contaminant is homogeneously distributed within the domain, the probability of it being cleaned by the flow of argon is proportional to its concentration. The concentration of X is then:

$$f_X(t) = \frac{q}{\frac{dN_{Ar}}{dt}} \left(1 - \exp \left\{ -\frac{1}{N_{Ar}} \frac{dN_{Ar}}{dt} \cdot t \right\} \right). \quad (C.3)$$

Expression C.2 can be rewritten as a function of the magnitudes used in text if we recall the ideal gas law $P = \frac{N_{Ar}}{V} K T$, so $N_{Ar} = \frac{P V}{K T}$, that is valid as long as $N_{Ar} \gg N_X$. Similarly, we obtain:

$$\frac{dN_{Ar}}{dt} = \frac{P}{K T} \frac{dV}{dt}. \quad (C.4)$$

And we can re-express eq. C.3 as:

$$f_X(t) = \frac{Q \cdot A}{P \cdot \Phi} \left(1 - \exp \left\{ -\frac{\Phi}{V} \cdot t \right\} \right), \quad (C.5)$$

where Q is the outgassing rate in units of $[\frac{P \cdot V}{A \cdot t}]$ and Φ is the flow rate in liters per unit time, as defined in text ($\Phi \equiv \frac{dV}{dt}$). A is the total outgassing area. The formula for the concentration $f_X(t)$ exhibits a global scaling upon changes of the outgassing rate Q , its time dependence being a function of the flow rate and total volume.

C.2 Power-law outgassing rate

A more realistic model for the outgassing of plastics is a power law, where $q(t) \propto t^{-1/2}$. The general solution of equation (C.1) is

$$N_X(t) = \exp \left\{ -\frac{dN_{Ar}}{dt} \cdot \frac{1}{N_{Ar}} \cdot t \right\} \left(\int_0^t \exp \left\{ \frac{dN_{Ar}}{dt} \cdot \frac{1}{N_{Ar}} \cdot \tau \right\} q(\tau) d\tau + c_1 \right). \quad (C.6)$$

Assuming again that the concentration is zero at $t = 0$ and taking the definition in text, under which $q(t) = Q_{10h} \cdot \frac{A}{K T} \cdot \sqrt{10/t}$, with t in hours, the previous expression can be written as

$$N_X(t) = \exp \left\{ -\frac{dN_{Ar}}{dt} \cdot \frac{1}{N_{Ar}} \cdot t \right\} \frac{\sqrt{10\pi} \cdot Q_{10h} \cdot \frac{A}{K T} \cdot \operatorname{erfi} \left(\sqrt{\frac{dN_{Ar}}{dt} \frac{1}{N_{Ar}}} \sqrt{t} \right)}{\sqrt{\frac{dN_{Ar}}{dt} \frac{1}{N_{Ar}}}}, \quad (C.7)$$

where erfi represents the error function. The concentration of X is then

$$f_X(t) = \exp \left\{ -\frac{dN_{Ar}}{dt} \cdot \frac{1}{N_{Ar}} \cdot t \right\} \frac{\sqrt{10\pi} \cdot Q_{10h} \cdot \frac{A}{KT} \cdot \operatorname{erfi} \left(\sqrt{\frac{dN_{Ar}}{dt} \frac{1}{N_{Ar}}} \sqrt{t} \right)}{\sqrt{\frac{dN_{Ar}}{dt} \frac{1}{N_{Ar}}} N_{Ar}}. \quad (\text{C.8})$$

Using the definitions of previous section we find:

$$f_X(t) = \exp \left\{ -\frac{\Phi}{V} \cdot t \right\} \frac{\sqrt{10\pi} \cdot Q_{10h} \cdot A \cdot \operatorname{erfi} \left(\sqrt{\frac{\Phi}{V}} \cdot \sqrt{t} \right)}{\sqrt{\frac{\Phi}{V}} P \cdot V}. \quad (\text{C.9})$$

C.3 Gas displacement during filling

Under the aforementioned ‘diffusion-dominated’ conditions, it is straightforward to write the evolution equation for contaminant X, assumed to be filling the chamber at $t = 0$ (air, for instance), as:

$$\frac{dN_X}{dt} = -\frac{dN_{Ar}}{dt} \cdot \frac{N_X}{N_{Ar}}, \quad (\text{C.10})$$

yielding the familiar solution:

$$f_X(t) = \exp \left\{ -\frac{\Phi}{V} \cdot t \right\}. \quad (\text{C.11})$$

C.4 Gas accumulation

If the outgassing element is oblivious to purification (as assumed in text for N_2), eq. C.1 is replaced by:

$$\frac{dN_X}{dt} = q(t). \quad (\text{C.12})$$

The solution is:

$$f_X(t) = \frac{KT}{PV} \int_0^t q(t') dt', \quad (\text{C.13})$$

or

$$f_X(t) = \frac{A}{PV} \int_0^t Q(t') dt', \quad (\text{C.14})$$

as a function of the main magnitudes used in text. When the outgassing decreases with time as $t^{-1/2}$, impurities accumulate in the system as $f_X \sim t^{1/2}$.